Research Square

Preprints are preliminary reports that have not undergone peer review.
They should not be considered conclusive, used to inform clinical practice,
or referenced by the media as validated information.

Soil-derived compound drought-hot events exert stronger constraints on global vegetation restoration than meteorological sources

Peng Sun

sun68peng@163.com

Zice Ma

https://orcid.org/0009-0006-0271-8085

Chunchen Wang

Donghua Chen

Yifan Zou

Article

Keywords: Compound drought–hot events, Stress-source divergence, Vegetation21 response trajectory, Attribution analysis, Nonlinear thresholds

Posted Date: August 31st, 2026

DOI: https://doi.org/10.21203/rs.3.rs-10596168/v1

License: This work is licensed under a Creative Commons Attribution 4.0 International License.
Read Full License

Additional Declarations: There is **NO** Competing Interest.

Soil-derived compound drought-hot events exert stronger constraints on global vegetation restoration than meteorological sources

Abstract

The frequency and intensity of compound drought-hot events have surged under climate warming, but the distinct roles of meteorological (MetDH) and soil-derived (SoilDH) stress in shaping vegetation response trajectories remain unknown. Here we show that SoilDH causes a 38% greater maximum loss and an 82% longer recovery time than MetDH, despite having a shorter response window. The resistance and recovery disparities between SoilDH and MetDH are amplified by higher soil organic carbon content but dampened by higher gross primary productivity, whereas the maximum loss disparity is governed by climatic background and anthropogenic activities. Critically, this difference exhibits non-linear intensification when the human activity index exceeds 0.10 or the vapor pressure deficit exceeds 0.26 kPa, indicating that human-induced pressure and atmospheric drought exacerbate the vulnerability of ecosystems to soil-derived stress. This divergence is most pronounced in croplands and arid regions, where biological buffering is limited. Our findings imply that assessments based solely on MetDH underestimate the ecological costs of SoilDH and overestimate recovery potential, distorting ecological damage evaluation. Future risk assessments must explicitly account for stress-source divergence to avoid misguided adaptation strategies.

Keywords: Compound drought–hot events; Stress-source divergence; Vegetation response trajectory; Attribution analysis; Nonlinear thresholds

Introduction

Global warming has sharply increased the frequency and intensity of compound drought–hot event (CDHE)[1,2], exemplified by the record-breaking 2022 events across the Yangtze River Basin, central-southern Europe, and the western United States[3,4,5,6]. These events cause widespread vegetation browning and yield losses that substantially exceed the sum of isolated droughts and heatwaves due to their synergistic amplification effects[7,8,9,10,11,12]. Therefore, accurate assessment of vegetation response trajectories under CDHE is critical for informing climate adaptation and mitigation strategies.

Nevertheless, current CDHE definitions remain predominantly meteorological (MetDH), relying on atmospheric variables such as temperature, vapor pressure deficit, and precipitation[2,13], whereas soil-based definitions (SoilDH) based on soil temperature and moisture have received far less attention[1]. Physiologically, MetDH primarily suppresses photosynthesis via stomatal limitations and canopy structural changes, whereas SoilDH directly impedes root water uptake and transpiration, thereby imposing distinct constraints on vegetation functioning[14,15,16]. Despite these fundamentally different pathways, no study has yet compared their differential effects on the full vegetation response trajectory, including resistance time (T_{res}), recovery time (T_{rec}), and maximum loss ($Loss_{max}$). These three metrics collectively characterize buffering capacity, damage severity, and post-stress recovery[17,18,19,20,21,22,23].

Neglecting the differences in vegetation response trajectories and greatly underestimating the ecological impacts of CDHE. Recent studies have shown that the productivity loss caused by SoilDH is on average 1.115 g C m^{-2} day^{-1} more than MetDH[15]. While recent studies have identified that vapor pressure deficit and soil moisture jointly regulate vegetation carbon losses[24,25,26], and that recovery lags differ across biomes[27,28], these investigations typically treat CDHE as a single stress type or focus on isolated environmental variables. Consequently, how background climatic

conditions, vegetation states, hydro-climatic anomalies, anthropogenic activities, and topography collectively mediate the divergent vegetation responses to MetDH and SoilDH remains unclear.

Here we construct separate Meteorological and Soil Compound Drought-Hot Indices (MetCDHI and SoilCDHI) using a copula function, and validate their ability to capture distinct physical characteristics. By integrating these indices with detrended Normalized Difference Vegetation Index residual data (hereafter, NDVI), we quantify the differences in T_{res}, T_{rec}, and $Loss_{max}$ between MetDH and SoilDH. We hypothesize that SoilDH induces substantially longer recovery times and greater maximum losses than MetDH, particularly in water-limited regions and croplands. To disentangle the underlying drivers, we couple an extreme gradient boosting (XGBoost) and SHapley Additive exPlanations (SHAP) framework with partial least squares structural equation models (PLS- SEM) to examine how background environmental conditions, vegetation state, hydro-climatic anomalies, anthropogenic activities, and topography jointly regulate this divergence. Our framework tests whether intrinsic ecosystem properties and external climatic-anthropogenic forcings exert distinct controls on resistance, recovery, and damage disparities, and seeks to identify critical thresholds beyond which SoilDH vulnerability escalates. This work aims to provide a mechanistic basis for differentiating stress sources in post-CDHE risk assessments.

Results

Physical divergence and intensification of MetDH versus SoilDH

To evaluate the ecological fidelity of our copula-based indices, we first validated their ability to capture the respective signatures of atmospheric and soil water-heat coupling. While the optimal copula types exhibit marked spatial heterogeneity to accommodate diverse dependency structures between drought and heat (Supplementary Fig. 1), the derived MetCDHI and SoilCDHI showed robust correlations with their constituent single-variable anomalies (Fig. 1). Globally,

MetCDHI was tightly coupled with the Standardised Precipitation Index (SPI) (R = 0.79) and the Standardised Temperature Index (STI) (R = -0.77), confirming its effectiveness in representing atmospheric dry-hot forcing (Fig. 1a, b). In contrast, SoilCDHI exhibited even stronger associations with the Standardised Soil Moisture Index (SSMI) (R = 0.87) and the Standardised Soil Temperature Index (SSTI) (R = -0.84) (Fig. 1c, d). This pattern is particularly pronounced in low-latitude regions and for croplands, confirming that our indices faithfully represent the compound stress signals experienced by MetDH and SoilDH, respectively.

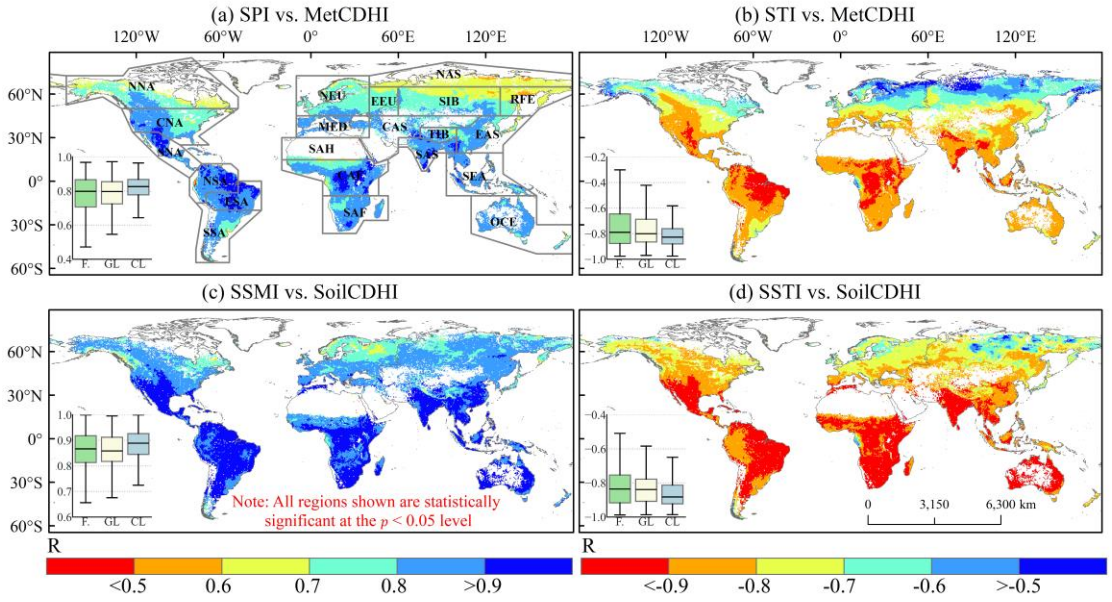


Fig. 1 | Global spatial correlations between single-variable indices and compound drought-hot indices. a, b, Spatial distribution of Pearson correlation coefficients (R) between the Standardized Precipitation Index (SPI) and Standardized Temperature Index (STI) with the meteorological compound drought-hot index (MetCDHI), respectively. **c, d,** Similar to **a, b,** but showing correlations between the Standardized Soil Moisture Index (SSMI) and Standardized Soil Temperature Index (SSTI) with the soil-derived compound drought-hot index (SoilCDHI). Inset boxplots in **a–d** display the distribution of R across different vegetation functional types. Coloured grid cells indicate statistically significant correlations at $p < 0.05$. The IPCC AR6 reference region boundaries are indicated in **a**.

In addition to statistical correlation analysis, we also examined the record-breaking extreme CDHE in 2022 and found that the affected area of SoilDH expanded relative to that of MetDH. A pronounced asynchrony between the two CDHE types is nevertheless evident. During July and August 2022, SoilDH surpassed MetDH in both spatial extent and intensity, with its footprint expanding beyond that

of the atmosphere (Fig. 2a–c vs. 2d–f). This direct physical divergence confirms that MetDH and SoilDH operate through distinct mechanisms. SoilDH is less frequent but longer and more intense than MetDH, suppressing vegetation growth (Supplementary Figs. 2), whereas MetDH elicits compensatory responses (Supplementary Figs. 3). Thus, they must be assessed separately.

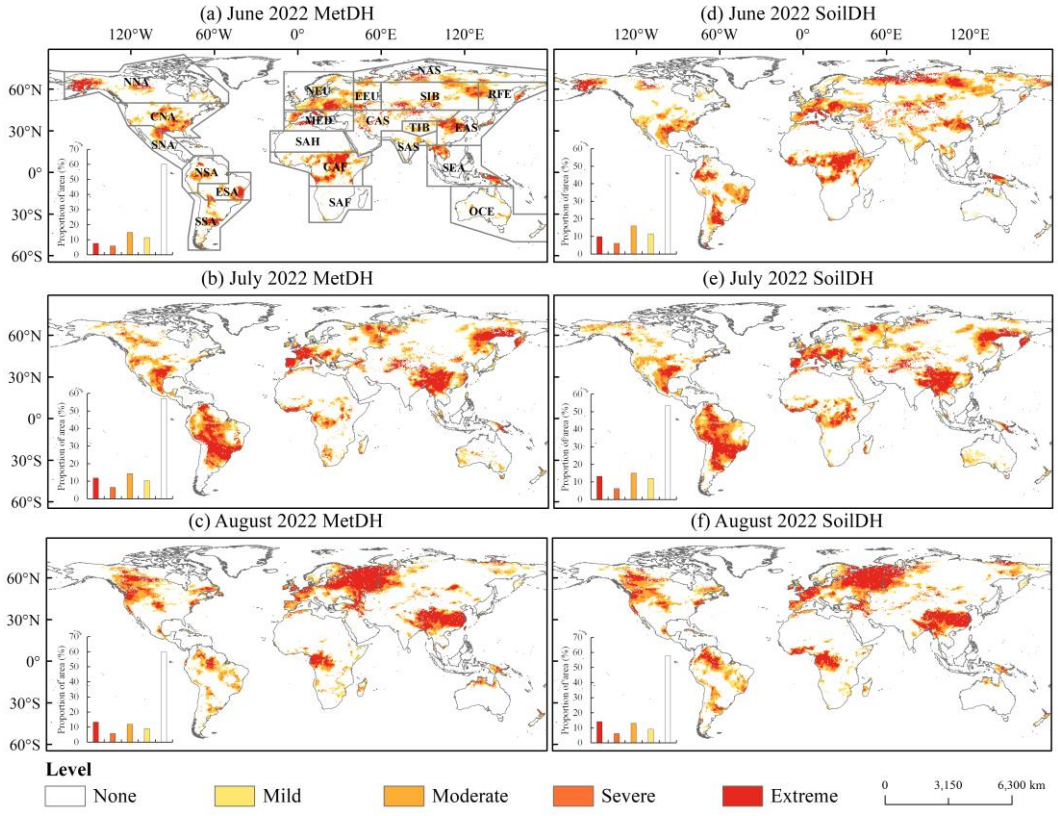


Fig. 2 | Spatial patterns of MetDH and SoilDH during June-August 2022. a–c, Meteorological compound drought-hot events (MetDH) categorized by intensity levels for June, July and August 2022. **d–f,** Corresponding spatial patterns of soil-derived compound drought-hot events (SoilDH) for the same period. Inset bar charts display the proportion of area affected by each intensity category. The IPCC AR6 reference regions are shown in **a**.

Over the past four decades (1982–2022), global CDHE has intensified markedly, yet vegetation greenness has simultaneously increased across much of the globe (Fig. 3). We found that 93.7% of vegetated areas experienced MetDH intensification (64.1% significant) and 90.5% experienced SoilDH intensification (58.3% significant), whereas NDVI increased over 54.7% of the vegetated areas (31.2% significant) (Fig. 3a–c). Significant CDHE intensification is concentrated in Europe (Northern Europe, NEU; Mediterranean, MED), East Asia (EAS) and eastern South America (ESA), whereas notable greening occurs in South Asia (SAS), EAS and the MED (Fig. 3a–c).

Across climatic zones, greening fractions ranged from 35.8% in HU regions to 22.8% in AR regions despite comparable CDHE intensification (Fig. 3d–f). Cropland (CL) showed the strongest intensification of both CDHE types yet the largest greening fraction (46.7%), whereas forest (F.) displayed the weakest greening signal (Fig. 3g–i). This decoupling suggests that apparent greening may mask declining stress tolerance, motivating our quantification of the full response trajectory, including T_{res}, T_{rec} and $Loss_{max}$, to reveal the ecological costs of SoilDH versus MetDH.

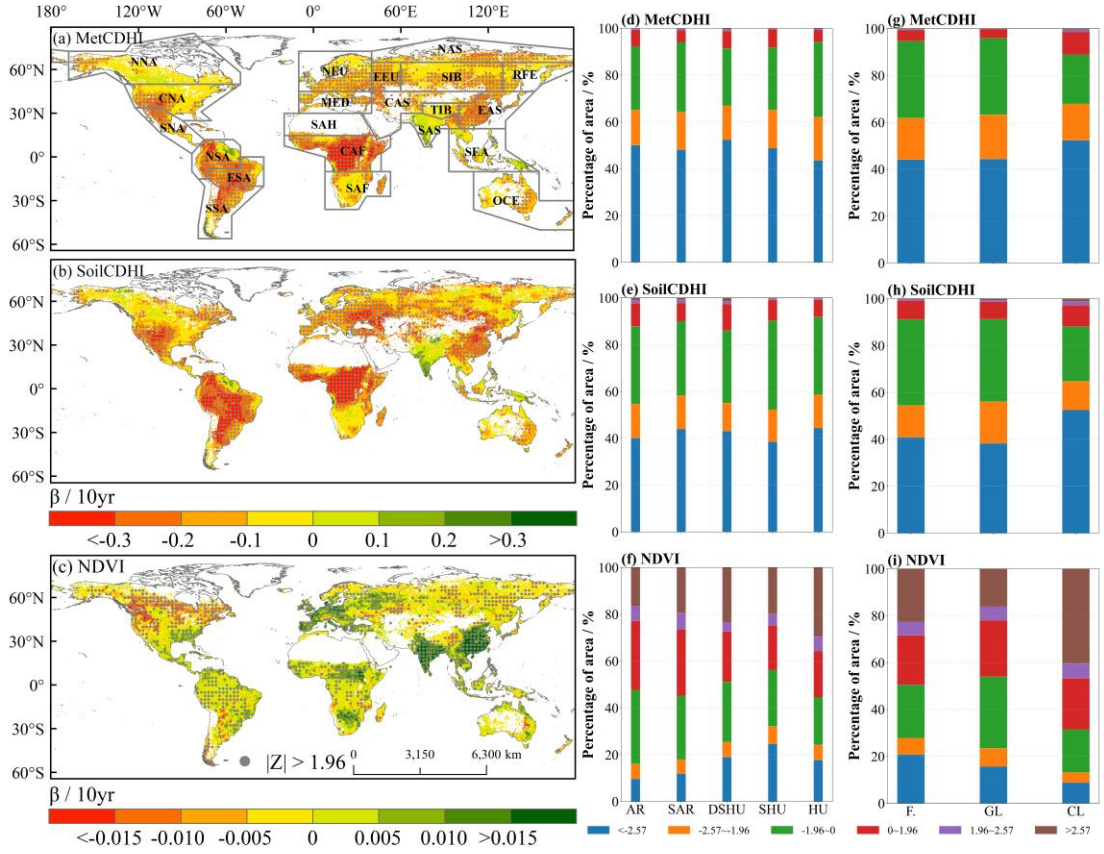


Fig. 3 | Spatiotemporal trends of MetCDHI, SoilCDHI, and NDVI during 1982-2022. a–c, Global trends of MetCDHI, SoilCDHI, and Normalized Difference Vegetation Index (NDVI). **d–f,** Area-proportional trends across five climate zones (AR, arid; SAR, semi-arid; DSHU, dry sub-humid; SHU, sub-humid; HU, humid). **g–i,** Trends across three vegetation functional types (F., forest; GL, grassland; CL, cropland). Grey dots denote statistically significant trends (|Z| > 1.96). The IPCC AR6 reference regions are indicated in **a**.

Accumulated lag effect reveals greater vegetation costs brought by SoilDH

Concurrent NDVI–CDHI correlations were unexpectedly weak, with significant positive associations in only 27.2% and 35.1% of vegetated areas for MetCDHI and

SoilCDHI respectively ($p < 0.05$; Fig. 4a-b). At the global mean scale, NDVI correlated negatively with MetCDHI (R = -0.041), whereas it correlated weakly positively with SoilCDHI (R = 0.024), a pattern that contradicts the observed intensification of CDHE (Fig. 4a-b). This apparent decoupling motivated our examination of cumulative lag effects.

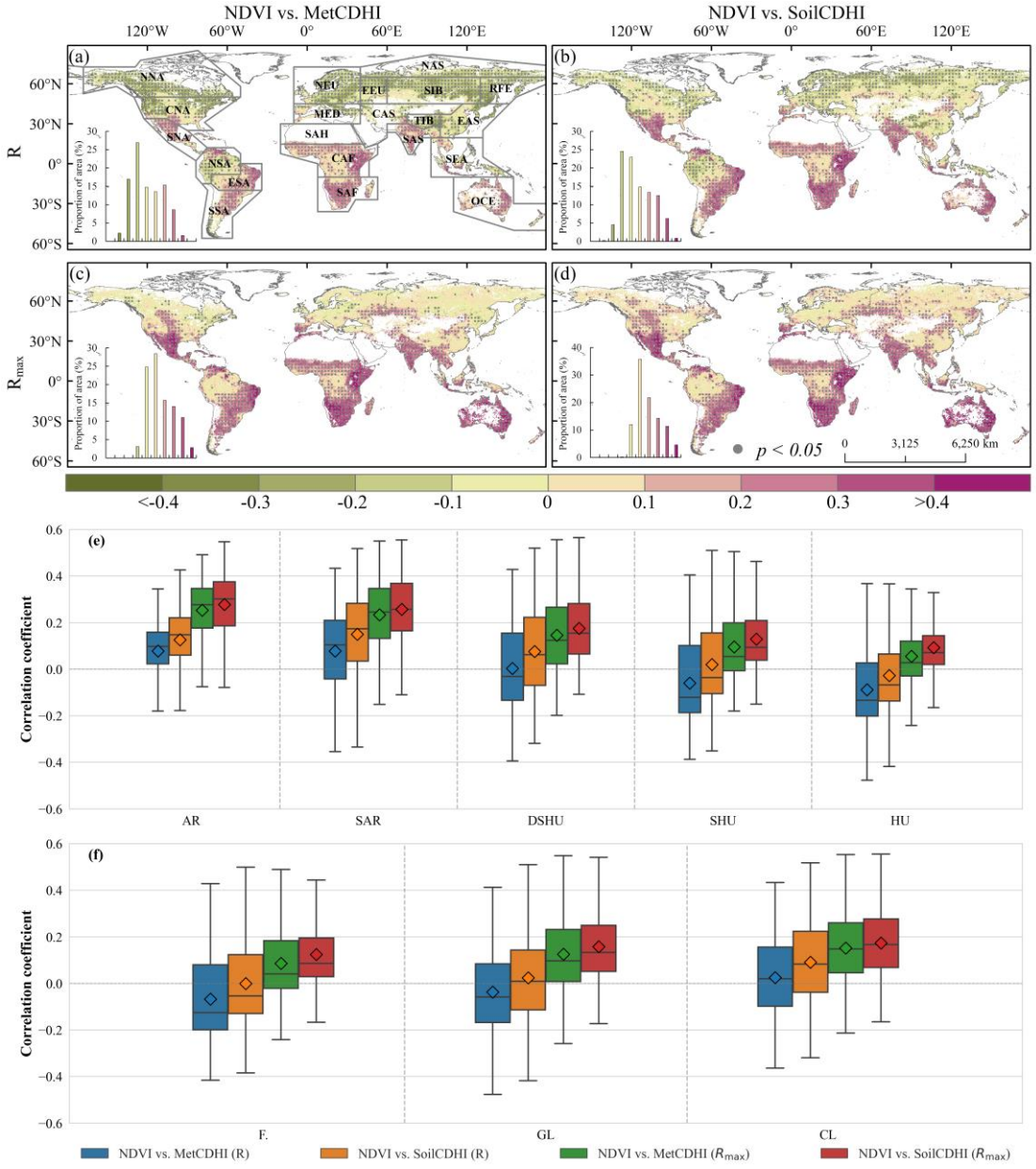


Fig. 4 | Divergent vegetation sensitivity to MetDH and SoilDH driven by cumulative lag effects. a, b, Spatial patterns of contemporaneous Pearson correlations (R) between NDVI and MetCDHI **(a)** and SoilCDHI **(b)**. **c, d,** Maximum correlations (R_{max}) between NDVI and MetCDHI **(c)** and SoilCDHI **(d)** when incorporating accumulated lags. **e, f,** Boxplots comparing R and Rmax distributions across climate zones **(e)** and vegetation functional types **(f).** Grey dots indicate significance at $p < 0.05$. The IPCC AR6 reference regions are shown in **a**.

Accounting for accumulated lag effects fundamentally altered these relationships (Fig. 4c–d). The global R_{max} values between NDVI and MetCDHI / SoilCDHI surged to 0.107 / 0.141, with a significant positive correlation increasing to 46.0% / 55.9% (Fig. 4c–d). The optimal lag time was consistently shorter for SoilCDHI (5.4 months) than for MetCDHI (7.1 months; Supplementary Fig. 4). Spatially, the strongest accumulated lag effects for both indices occurred in OCE (R_{max} = 0.326 and 0.355), whereas the longest lag time, exceeding 10 months for MetCDHI and 7.5 months for SoilCDHI, was observed in high-latitude regions including Siberia (SIB), northern North America (NNA) and North Asia (NAS) (Supplementary Fig. 5). Across climate zones, AR and SAR regions had the strongest cumulative responses to SoilCDHI (R_{max} = 0.277 and 0.257) but the shortest lags (3.4 and 2.8 months), whereas HU regions showed the weakest effects (R_{max} = 0.055 and 0.092) and longest lags (7.3 and 5.7 months; Fig. 4e; Supplementary Fig. 4c). Among vegetation functional types, CL had the highest cumulative responses (R_{max} = 0.152 and 0.173; lags 4.5 and 3.4 months), whereas F. had the lowest (R_{max} = 0.085 and 0.124; lags 7.1 and 5.4 months; Fig. 5f; Supplementary Fig. 3d). NDVI thus responds more rapidly yet more strongly to SoilDH than to MetDH, indicating that concurrent analyses severely underestimate the true vegetation cost of CDHE.

Quantifying the full vegetation response trajectories revealed substantial disparities between the MetDH and SoilDH in terms of T_{res}, T_{rec}, and $Loss_{max}$ (Fig. 5). Global mean T_{res} increased from 4.0 ± 2.0 months under MetDH to 6.4 ± 0.7 months under SoilDH, a greater than 60% prolongation affecting 88.7% of vegetated areas (Fig. 5a–c). T_{rec} rose from 3.8 ± 2.3 months to 6.9 ± 2.1 months, with 89.7% of areas showing prolonged recovery (Fig. 5d–f). $Loss_{max}$ under SoilDH (0.047 ± 0.022) was 1.38-fold higher than under MetDH (0.034 ± 0.028), affecting 77.6% of vegetated areas (Fig. 5g–i). SoilDH therefore inflicts deeper damage and delays recovery despite a shorter response window.

The magnitude of these disparities varied considerably across climate zones and

vegetation types (Supplementary Fig. 6). AR regions experienced the largest ΔT_{res} (2.7 months) and ΔT_{rec} (3.8 months) (Supplementary Fig. 6a-c). Among vegetation functional types, grassland (GL) showed the largest ΔT_{rec} (3.5 months) with the longest T_{rec} (7.3 months), whereas CL exhibited the largest $\Delta Loss_{max}$ (0.017), highlighting their acute vulnerability to SoilDH. F. showed the smallest differences across all metrics (Supplementary Fig. 6e-f). The trade-off between prolonged T_{res} and T_{rec} underscores the role of intrinsic ecosystem properties[29]. We next disentangled the drivers of these divergent responses using an integrated attribution and path analysis framework.

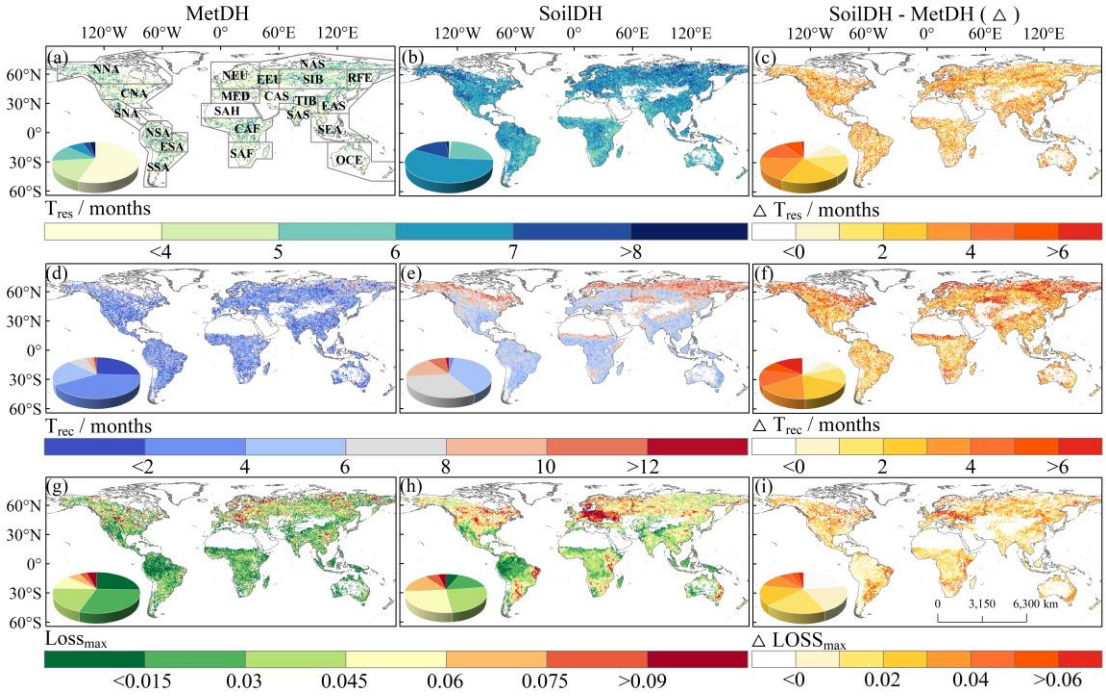


Fig. 5 | Global patterns of vegetation response to MetDH and SoilDH. a–c, Spatial distributions of resistance time (T_{res}) for MetDH **(a)**, SoilDH **(b)**, and their difference (ΔT_{res} = SoilDH – MetDH) **(c). d–f,** Same as **a–c,** but for recovery time (T_{rec}). **g–i,** Same as **a–c,** but for maximum vegetation loss ($Loss_{max}$). Inset pie charts denote the proportion of global vegetated area in each corresponding category. The IPCC AR6 reference regions are indicated in **a**.

Drivers and critical thresholds of divergent vegetation responses to SoilDH versus MetDH

To disentangle the drivers of these divergent vegetation responses, we employed an XGBoost-SHAP interpretable framework followed by PLS-SEM path analysis (Fig. 6–8; Supplementary Figs. 7-10). Our results revealed that ΔT_{res} and ΔT_{rec} share highly

similar dominant controls, whereas $\Delta Loss_{max}$ exhibits a distinctly different pattern.

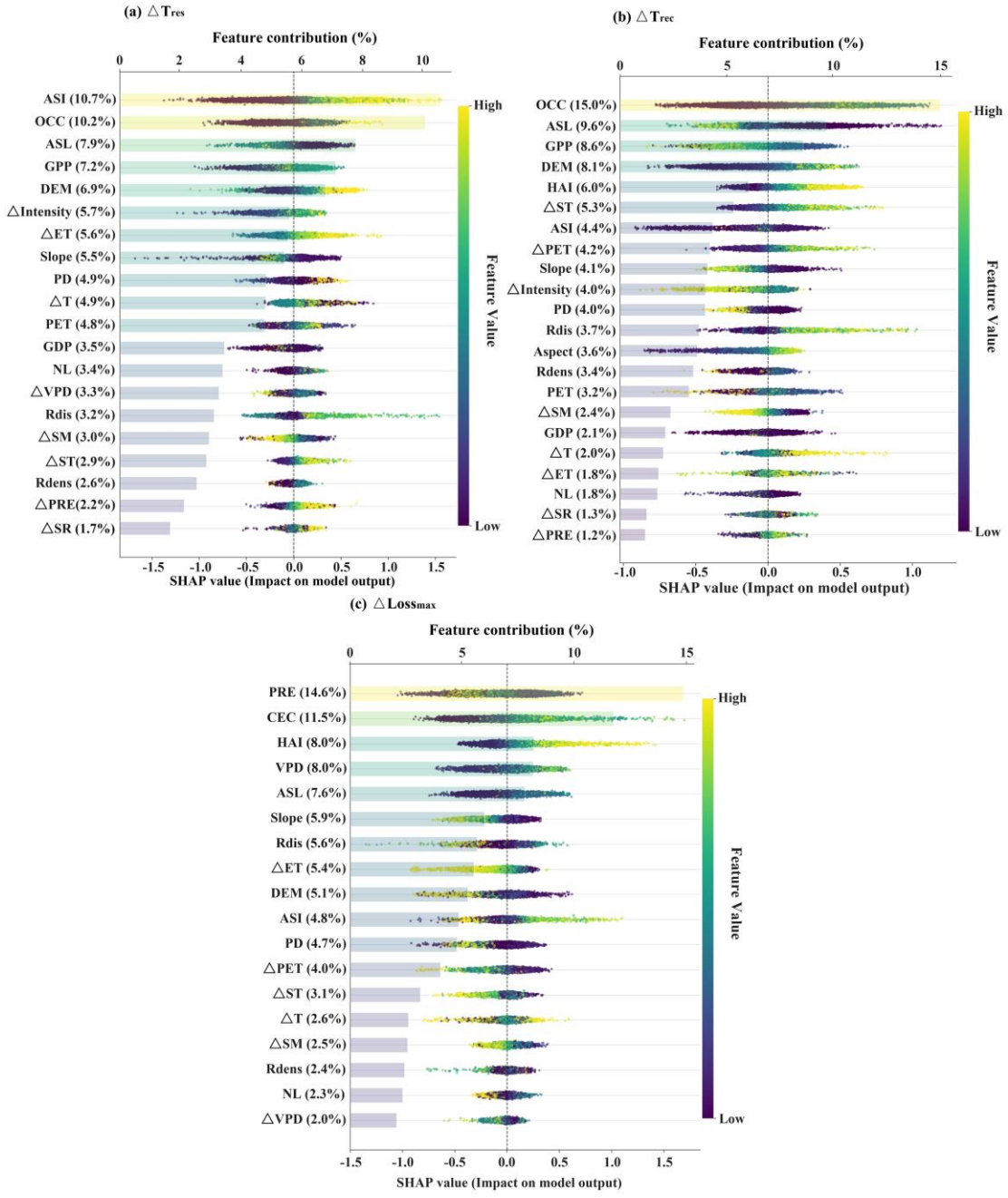


Fig. 6 | SHAP-based feature importance for divergent vegetation response predictions. a–c, SHAP feature attribution analysis for the XGBoost-predicted differences in resistance time **(a)**, recovery time **(b)**, and maximum loss **(c)** between SoilDH and MetDH. Bar lengths represent global feature importance (mean absolute SHAP value). The colour scale indicates feature magnitude, and the x-axis denotes the direction and magnitude of the SHAP impact. Positive SHAP values indicate a positive contribution to the response difference. Abbreviations of the driver variables are defined in Supplementary Table 3.

Our attribution analysis reveals a clear mechanistic dichotomy, with ΔT_{res} and ΔT_{rec} sharing highly similar dominant controls primarily including anthropogenic

species increments (ASI: 10.7% and 4.4%), organic carbon content (OCC: 10.2% and 15.0%), anthropogenic species losses (ASL: 7.9% and 9.6%), gross primary productivity (GPP: 7.2% and 8.6%) and Elevation (DEM: 6.9% and 8.1%) (Fig.6a-b). Spatially, the positive effects of ASI were concentrated in mid-to-high latitudes, whereas the negative effects of OCC and ASL dominate regions including Sahara (SAH), Oceania (OCE), southern North America (SNA), Central Asia (CAS) and southern Africa (SAF) (Supplementary Fig. 7a–l). By contrast, $\Delta Loss_{max}$ was governed by an entirely different set of drivers, led by precipitation (PRE: 14.6%), cation exchange capacity (CEC: 11.5%), human activity intensity (HAI: 8.0%) and vapor pressure deficit (VPD: 8.0%) (Fig.6c). The negative effects of PRE and CEC were widespread across tropical regions (Southeast Asia, SEA; North Asia, NAS and ESA), whereas the positive effect of HAI was particularly pronounced in the MED (Supplementary Fig. 7m–r). This dichotomy persisted across climate zones and vegetation functional types, with OCC prevailing in AR and SAR for both ΔT_{res} and ΔT_{rec}, while PRE dominated $\Delta Loss_{max}$ across all zones (Supplementary Figs. 8-9).

Partial dependence plots revealed nonlinear thresholds with clear management implications (Fig. 7). For ΔT_{res}, the SHAP values transition from negative to positive when ASI exceeds 97.30 species (Fig.7a). For both ΔT_{res} and ΔT_{rec}, the SHAP values turned positive when OCC surpassed 1.23% and 2.15%, respectively (Fig.7b, g). For $\Delta Loss_{max}$, SHAP values increase continuously when CEC exceeds 12.46 $cmol(+)\cdot kg^{-1}$, whereas the opposite effect occurs when Slope exceeds 0.44° (Fig.7n, r). When ΔIntensity exceeds 0.97 and ΔST exceeds 0.34 $°C\cdot month^{-1}$, the SHAP values for both ΔT_{res} and ΔT_{rec} turn from negative to positive, but the increase is much more pronounced for ΔST, suggesting that intensifying CDHE has a greater deteriorating effect on recovery than on resistance (Fig.7f, l). The SHAP value for PRE becomes positive once precipitation exceeds 340.07 mm, and then turns negative again when precipitation surpasses 1,194.47 mm (Fig. 7m). This indicates that $\Delta Loss_{max}$ reaches its maximum within the intermediate humidity range, while being smaller under both

extremely arid and extremely humid conditions. Furthermore, when HAI exceeds 0.10 or VPD surpasses 0.26 kPa, SHAP values increase sharply, underscoring that human disturbance and atmospheric aridity can substantially amplify the ecological losses induced by SoilDH (Fig.7o, p).

PLS-SEM path analysis further resolved the direct and indirect pathways underlying these disparities (Fig. 8; Supplementary Fig. 10). For ΔT_{res} and ΔT_{rec}, OCC exerted significant positive direct effects (0.037 and 0.114), whereas GPP showed strong negative direct effects (−0.081 and −0.272), indicating that carbon-rich soils buffer SoilDH stress, while high productivity narrows the gap between stress types through enhanced recovery capacity (Fig.8a-b; Supplementary Fig. 10a-b). For $\Delta Loss_{max}$, HAI showed the strongest positive direct effect (0.105), PRE exhibited a significant negative direct effect (−0.066), and VPD amplified losses through both direct and indirect pathways (Fig.8c; Supplementary Fig. 10c). Collectively, these results demonstrate that the mechanisms governing ΔT_{res} and ΔT_{rec} are rooted in intrinsic ecosystem properties, whereas the $\Delta Loss_{max}$ is externally forced by atmospheric drought and anthropogenic pressure, with clear nonlinear thresholds that carry direct implications for adaptive management.

Discussion

To distinguish MetDH from SoilDH, we constructed copula-based indices (MetCDHI and SoilCDHI) and integrated them with long-term NDVI observations, an XGBoost-SHAP, and PLS-SEM. This framework allows us to quantify the divergent impacts of MetDH and SoilDH on vegetation response trajectories and to elucidate the ecological mechanisms governing the buffering-damage-recovery sequence. Cross-validation using four independent vegetation proxies confirms that our findings represent a robust and pervasive ecological phenomenon (Supplementary Fig. 11). All observations indicate that assessments based solely on MetDH inherently conceal the true costs imposed by SoilDH, underestimating the ecological impacts of

CDHE[2,13,16].

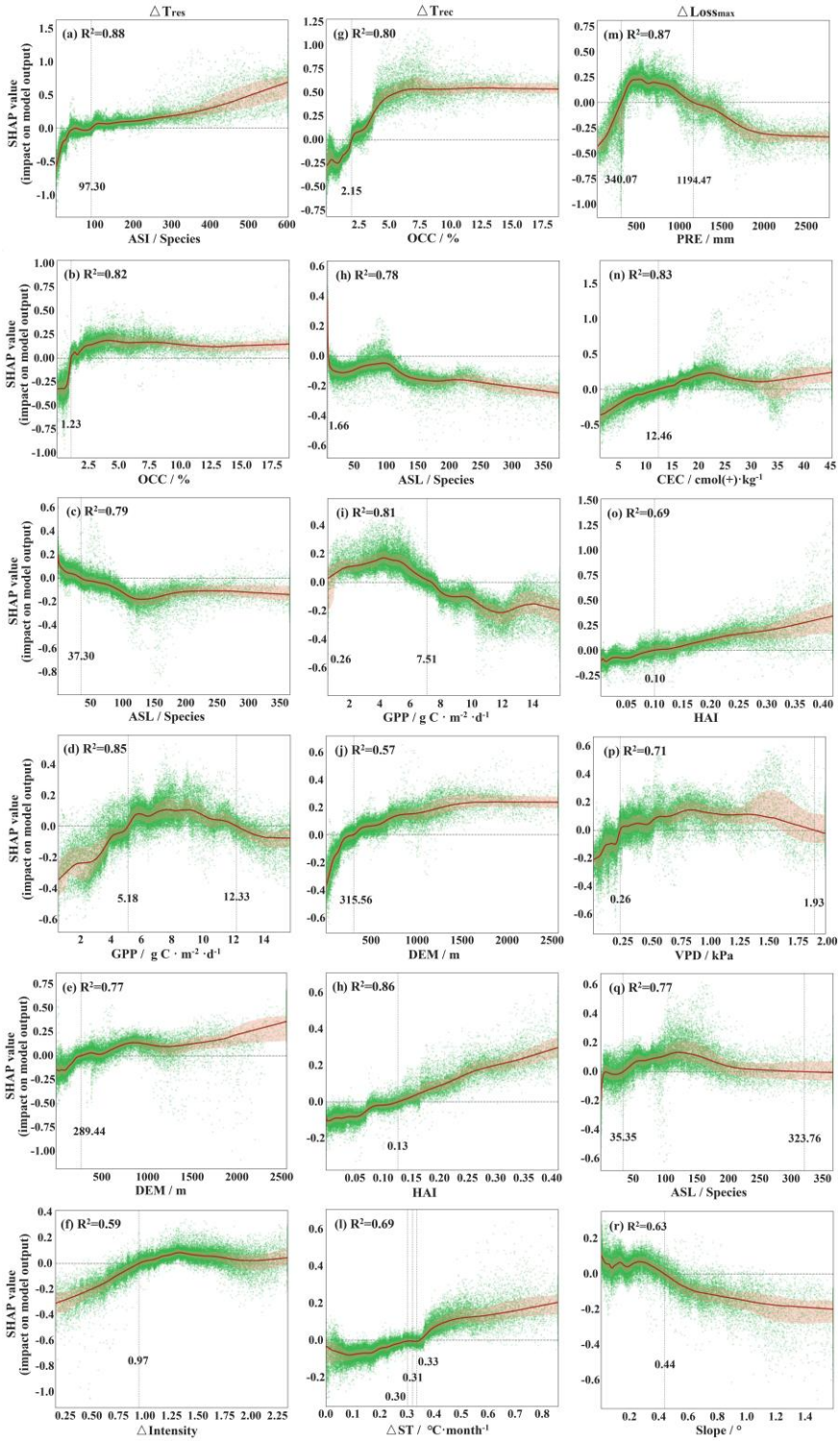


Fig. 7 | Nonlinear effects of key drivers on vegetation response differences. a–r, Partial dependence plots of SHAP values for the differences in resistance time (ΔT_{res}, left column), recovery time (ΔT_{rec}, middle column), and maximum loss ($\Delta Loss_{max}$, right column) against the respective driving variables (rows). Green scatter points show local SHAP values for individual samples. Deep red lines represent smoothed trends approximating central tendency, with red-shaded areas indicating 95% confidence intervals. Vertical dashed lines mark the zero-impact threshold (SHAP = 0). Abbreviations of the driver variables are defined in Supplementary Table 3.

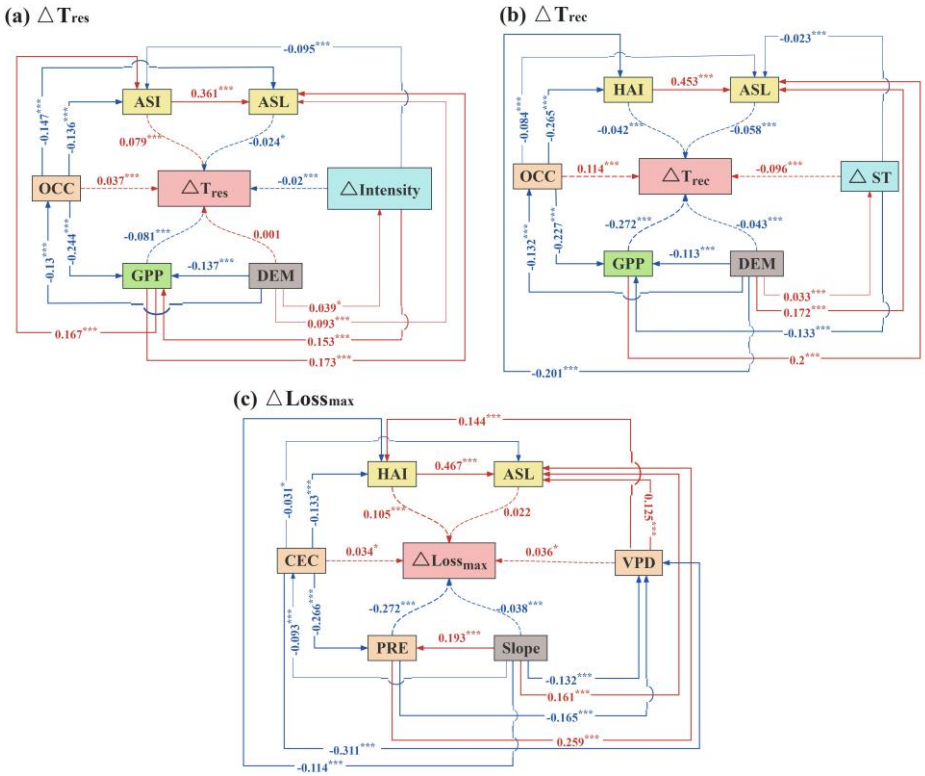


Fig. 8 | PLS-SEM pathways elucidating drivers of divergent vegetation responses to SoilDH versus MetDH. **a-c,** The PLS-SEM show the direct and indirect pathways regulating the ΔT_{res}, ΔT_{rec}, and $\Delta Loss_{max}$. Red and blue arrows indicate positive and negative standardized path coefficients, respectively. Solid lines denote indirect effects, whereas dashed lines represent direct effects. Asterisks denote statistical significance: *p < 0.05, **p < 0.01, and ***p < 0.001. Abbreviations of the driver variables are defined in Supplementary Table 3.

Our results demonstrate that SoilDH induces a 38% higher $Loss_{max}$ and an 82% longer T_{rec} than MetDH, despite a shorter cumulative response window (5.4 versus 7.1 months). This pattern of shorter exposure yet deeper and more prolonged damage points to fundamentally different physiological pathways. MetDH gradually suppresses canopy photosynthesis via elevated VPD, with moderate and short-lived damage from partial acclimation[7,30]. SoilDH rapidly interrupts root water supply and hydraulic conductance, causing severe and protracted damage[15, 16]. The 2022 events confirmed this pattern, with SoilDH expanding spatially beyond MetDH (Fig. 2), supporting the central role of soil hydrothermal coupling in driving ecosystem damage[3,5]. Recent studies have shown that SM deficits amplify productivity losses under CDHE[15], and that compound atmospheric and soil droughts further amplify global vegetation productivity loss[22]. Our findings extend these observations by

demonstrating that the disparity extends across the entire buffering-damage-recovery sequence.

Over the past four decades, CDHE intensified across over 90% of vegetated areas, yet NDVI increased over 54.7% of these areas (Fig.4). This decoupling does not imply that vegetation is immune to these stresses. Previous studies attributed this greening to rising CO_2 and warming[31]. However, Greening often comes at the cost of higher transpirational water consumption[32], with early-season water overuse causing later deficits that amplify sensitivity to SoilDH[33,34,35]. Our response indicators reveal the transfer process of this implicit cost: T_{res} under SoilDH extended by over 60%, but this does not indicate true stress tolerance. Rather, $Loss_{max}$ increased 1.38-fold and T_{rec} extended by approximately 82%. Chai et al.[20] found that flash droughts cause 9.0% greenness loss, much higher than the 5.3% under conventional droughts, with considerably longer recovery. Apparent greening therefore masks underlying degradation of tolerance to soil stress, and future adaptation assessments must integrate this hidden risk.

The changes between ΔT_{res} and ΔT_{rec} in the entire ecosystem reveal a trade-off between resistance and restoration, which is consistent with the observed trade-off between decreased resistance and restoration in drought studies[29]. Prolonged buffering against SoilDH depletes carbohydrate reserves and hydraulic safety margins, delaying subsequent regrowth[36]. AR regions, with the largest ΔT_{res} (2.7 months), consequently suffered the greatest ΔT_{rec} (3.8 months), indicating that extended resistance in water-limited systems comes at the expense of recovery capacity (Supplementary Fig. 6). Among vegetation functional types, F. showed the smallest $\Delta Loss_{max}$, reflecting buffering by deep root systems and hydraulic capacitance[37,38,39]. However, F. exhibited comparable or even greater ΔT_{res} and ΔT_{rec} relative to other types, consistent with evidence that species richness enhances resistance but may reduce resilience (Bai & Tang, 2024). GL showed the largest ΔT_{rec} (3.5 months) with the longest absolute recovery (7.3 months; Supplementary Fig. 6e), because shallow roots depend on the

312 0-7 cm soil layer; once dried, recovery relies entirely on subsequent rainfall[40]. CL
313 exhibited the largest $\Delta Loss_{max}$ (0.017; Supplementary Fig. 6f), highlighting acute
314 vulnerability during key phenological stages, compounded by management-induced
315 degradation of soil structure[41]. CL ecosystems lack effective biological buffering,
316 making them a key region for early warning.

317 Our attribution analysis reveals a clear dichotomy. ΔT_{res} and ΔT_{rec} are
318 predominantly controlled by intrinsic ecosystem properties, including OCC, ASL and
319 GPP. By contrast, $\Delta Loss_{max}$ is governed by external drivers, including PRE, HAI and
320 VPD (Fig. 6; Fig. 8). OCC exerts positive direct effects on both ΔT_{res} and ΔT_{rec},
321 indicating that carbon-rich soils buffer SoilDH stress through enhanced water
322 retention[42,43]. GPP shows strong negative direct effects, suggesting that highly
323 productive vegetation, despite facing a carbon and water trade off, possesses stronger
324 recovery capacity that narrows the gap between stress types[22,44]. For $\Delta Loss_{max}$, the
325 dominance of PRE, HAI and VPD confirms that external forcing determines damage
326 magnitude[16], implying that even well-buffered ecosystems remain vulnerable once
327 critical thresholds are crossed.

328 The identification of clear nonlinear thresholds is practically significant. When
329 OCC exceeds 1.23% and 2.15%, its influence on ΔT_{res} and ΔT_{rec} shifts from
330 suppressing to promoting. When ASI exceeds 97.30 species, its effect on ΔT_{res}
331 smilarly turns positive. These thresholds suggest that OCC and ASI confer limited
332 buffering until critical levels are reached[42,43,45]. More critically, when HAI exceeds
333 0.10 or VPD surpasses 0.26 kPa, $\Delta Loss_{max}$ increases sharply, indicating that
334 anthropogenic disturbance and atmospheric aridity trigger a nonlinear leap in
335 vulnerability[1,16,46]. Precipitation exerts unimodal control on $\Delta Loss_{max}$, with the
336 greatest impact at intermediate humidity. Such transitional zones, where vegetation is
337 neither drought-adapted nor moisture-buffered, are the most vulnerable. This
338 discovery provides a key scientific basis for future compound disaster risk
339 management, that is, priority should be given to identifying and strictly monitoring

fragile agro pastoral ecotones and AR region edges with HAI greater than 0.10 or VPD greater than 0.26 kPa.

Several limitations warrant consideration. Our 0.5° resolution smooths local heterogeneity, especially in topographically complex regions (MED and TIB). T_{rec} based on NDVI recovery may underestimate functional recovery, as carbon and water fluxes typically lag behind greenness recovery[47,48,49]. The thresholds identified are empirical and require validation through mechanistic models and long-term observations. Future work should integrate multi-source remote sensing, flux observations and land-surface models, incorporating stress-type discrimination into early-warning systems to inform precise ecological management under increasingly severe SoilDH.

Our results reveal that vegetation response to SoilDH incurs substantially higher ecological costs than to MetDH: $Loss_{max}$ is 38% higher, T_{rec} is 82% longer, and the cumulative response window is 1.7 months shorter. In addition, $\triangle T_{res}$ and $\triangle T_{rec}$ are predominantly governed by intrinsic ecosystem properties, whereas the $\triangle Loss_{max}$ is driven by external climatic and anthropogenic forcing. Critically, both the HAI and VPD exhibit nonlinear thresholds, beyond which ecosystem vulnerability to SoilDH increases sharply. These findings reveal ecophysiological mechanisms behind divergent vegetation responses to SoilDH and MetDH, highlighting that future risk assessments must account for stress-source differences, especially in CL and AR regions, to inform restoration strategies under global change.

Methods

Data sources and pre-processing

This study uses multiple datasets, with details on sources, resolution, temporal coverage, and roles given in Supplementary Table 1. Hourly total precipitation (PRE), surface net solar radiation (SR), total evaporation (ET), potential evaporation (PET),

2m temperature (T), 2m dewpoint temperature (T_d), 0-7cm soil moisture (SM), and soil temperature (ST) were extracted from the ERA5-Land reanalysis for the period 1982–2022 and subsequently aggregated to monthly time steps. Monthly 2-m maximum temperature (T_{max}) and 0-7cm maximum soil temperature (ST_{max}) for T and ST. Relative humidity (RH) and vapor pressure deficit (VPD) was calculated from T and T_d following Yuan et al.[30]. The ERA5-Land dataset has been widely validated and extensively employed in global extreme event and hydroclimatic studies[33,50,51].

From the Harmonized World Soil Database[52], we extracted soil properties, including bulk density (SBD), sand content (SAND), silt content (SILT), clay content (CLAY), pH, cation exchange capacity (CEC), organic carbon content (OCC), and carbon-to-nitrogen ratio (CNR), as key controls on water movement, retention, and nutrient availability[42,46,53]. Vegetation dynamics were primarily characterised using the PKU GIMMS normalized difference vegetation index (NDVI). A key advantage of this dataset is its effective correction of long-term uncertainty caused by NOAA satellite orbit drift and AVHRR sensor degradation, ensuring high consistency of NDVI time series from 1982 to 2022[54]. The derived response metrics were validated against independent GLASS products, and the NDVI, leaf area index (LAI), gross primary productivity (GPP) and net primary productivity (NPP) from the same GLASS dataset were additionally used as covariates in the attribution analysis. Land use and land cover change (LUCC) data from the ESA-CCI product were reclassified into three vegetation functional types: forest (F.), grassland (GL) and cropland (CL), and only pixels that experienced no land-use change during the study period were retained to isolate climatic effects[55] (Supplementary Fig. 12a).

Anthropogenic variables, namely population density (PD)[56], gross domestic product (GDP)[57], nighttime lights (NL)[58], road distance (R_{dis}), road density (R_{dens}) and the continuous terrestrial human activity intensity (HAI)[59], were sourced from the GlobPOP, downscaled GDP, MVNL, GRIP and global HAI datasets, respectively. Topographic elevation (DEM), slope, aspect were derived from GTOPO30, and

biodiversity metrics including native species richness (N), anthropogenic species increments (ASI) and anthropogenic species losses (ASL) were taken from the Level-8 hexagonal global grid system. All datasets were harmonised to a common 0.5° spatial grid. For existing gridded products, continuous variables were resampled using bilinear interpolation, whereas categorical layers were resampled using nearest neighbour[60]. Biodiversity vector data were rasterised by assigning the value at each grid-cell centre to the corresponding cell. Temporally varying predictors used in the attribution analysis were aggregated as multi-year averages over the study period to serve as static covariates, alongside inherently time-invariant properties such as soil and topographic attributes.

We further calculated the aridity index (AI) from the multi-year mean Pre and PET, and classified global land areas into five climatic zones: arid (AR, AI < 0.05), semi-arid (SAR, 0.05–0.20), dry sub-humid (DSHU, 0.20–0.50), sub-humid (SHU, 0.50–0.65), and humid (HU, > 0.65)[61] (Supplementary Fig. 12b). Regional analyses were based on the IPCC AR6 WGI reference regions[62], which included 21 sub-regions: Northern North America (NNA), Central North America (CNA), Southern North America (SNA), Northern South America (NSA), Eastern South America (ESA), Southern South America (SSA), Northern Europe (NEU), Mediterranean (MED), Eastern Europe (EEU), Sahara (SAH), Central Africa (CAF), Southern Africa (SAF), Central Asia (CAS), Tibetan Plateau (TIB), North Asia (NAS), Siberia (SIB), Russian Far East (RFE), East Asia (EAS), South Asia (SAS), Southeast Asia (SEA), and Oceania (OCE) (Supplementary Fig. 12a).

Analytical framework

Supplementary Fig. 13 provides a schematic overview of the full methodological workflow. The analysis comprises three sequential steps. First, we construct copula-based indices (MetCDHI and SoilCDHI) to characterise meteorological (MetDH) and soil-derived (SoilDH) compound drought-hot events. Second, we

quantify vegetation response trajectories for each stress type, including resistance time (T_{res}), recovery time (T_{rec}) and maximum loss ($Loss_{max}$), while explicitly accounting for accumulated lag effects. Third, we attribute the divergences between MetDH and SoilDH (ΔT_{res}, ΔT_{rec} and $\Delta Loss_{max}$) using an integrated XGBoost-SHAP and PLS-SEM framework.

Definition and characterisation of compound drought-hot events

We distinguished MetDH and SoilDH using different variable sets. For MetDH, We calculated the Standardised Precipitation Index (SPI) from PRE and the Standardised Temperature Index (STI) from T, fitting the SPI to a gamma distribution and the STI to a normal distribution, before standardising both to a standard normal distribution[63]. For SoilDH, we computed the Standardised Soil Moisture Index (SSMI) and Standardised Soil Temperature Index (SSTI) from SM and ST using the same procedure[64,65].

To capture the joint dependence between drought and high temperature, we constructed a copula-based joint distribution at each grid cell. The optimal copula family (Frank, Clayton, Gumbel, Gaussian, Student's t) was selected by Akaike Information Criterion (Supplementary Fig. 14). The joint cumulative probability was then standardised to obtain the MetCDHI and SoilCDHI indices[62]. An event is defined when CDHI < -0.5 (i.e. more than half a standard deviation below normal)[66]. This threshold is extensively applied in research on extreme climate events, and is physically equivalent to percentile-based standards[67,68,69]. Using a standardized classification framework, CDHE was divided into four intensity levels (Supplementary Tab. 2).

For each identified CDHE, three metrics were computed respectively for MetDH and SoilDH. Duration was defined as the number of consecutive months with CDHI < −0.5; intensity was calculated as the mean absolute CDHI during each event; frequency was computed as the total number of events divided by the number of years

from 1982 to 2022. For NDVI loss events, we adopted a similar method as CDHE, with a detrended NDVI falling below by 0.1SD as the event threshold[17], to ensure direct comparability between climate stress indicators and vegetation response indicators[17]. The calculation method for detrended NDVI is detailed in section 2.2.2.

Quantifying Vegetation Response Trajectories

To remove seasonal and long-term trends, we applied Seasonal-Trend decomposition using Loess (STL) to the monthly NDVI time series, retaining the residual anomaly for all subsequent analyses[70,71,72]. Because vegetation responses to antecedent stress exhibit legacy effects, we first quantified the accumulated lag effect[73,74,75,76]. For each pixel and stress type, we calculated the accumulated CDHI over antecedent periods from 1 to 12 months (k = 1,…,12) as the mean stress intensity over the current and preceding k-1 months. We then computed the Pearson correlation between the detrended NDVI residual and each accumulated CDHI series. The optimal cumulative lag for each pixel was identified as the lag time corresponding to the maximum correlation coefficient (R_{max}), ensuring that the identified lag reflects a biologically plausible stress–response relationship rather than a statistically fortuitous association[77].

Based on our accumulated lag analysis, which showed that the optimal lag times for the vast majority of vegetated areas fell within 12 months (Supplementary Fig. 4), we set a 12-month search window following each event onset to identify the timing of the minimum NDVI residual. The T_{res} was then defined as the duration from event onset to that minimum. The $Loss_{max}$ was calculated as the difference between the minimum NDVI anomaly and a local recovery threshold (i.e. −0.1 × standard deviation of non-stressed NDVI residuals)[17]. Recovery time (T_{rec}) was the number of months from the minimum to the first month when the NDVI residual reached or exceeded the recovery threshold for two consecutive months, and events not recovering within 24 months were excluded[20]. For MetDH, we retained only events

where SoilCDHI remained above −0.5 throughout the full response window to isolate atmospheric forcing. For each pixel, final T_{res}, T_{rec} and $Loss_{max}$ were averaged over all valid events.

Attribution of Divergent Vegetation Response

To disentangle the mechanisms driving the divergent vegetation responses to SoilDH versus MetDH, we defined three response-difference metrics as the core dependent variables: $\triangle T_{res}$ (SoilDH-induced Tres minus MetDH-induced Tres), $\triangle T_{rec}$ (SoilDH-induced Trec minus MetDH-induced T_{rec}), and $\triangle Loss_{max}$ (SoilDH-induced $Loss_{max}$ minus MetDH-induced $Loss_{max}$). A comprehensive suite of 52 candidate drivers was compiled across six categories: background environmental conditions, vegetation state, hydro-climatic anomalies, vegetation characteristics, and anthropogenic activities (Supplementary Tab. 3).

Given that the three response-difference metrics may be governed by distinct regulatory mechanisms, we performed an independent three-step screening procedure for each dependent variable to identify the most relevant predictor subsets. First, we retained only those predictors that showed a significant correlation with the target variable ($p < 0.05$; Supplementary Fig. 14). Second, we removed variables with high collinearity using a correlation coefficient threshold ($|R| > 0.6$), retaining the predictor that exhibited a stronger correlation with the response variable in cases of high pairwise correlation[78] (Supplementary Figs. 14–15). Third, we applied an iterative variance inflation factor (VIF) analysis, sequentially excluding predictors with VIF > 5 until all remaining variables satisfied the VIF criterion[79] (Supplementary Tab. 4). This procedure yielded final predictor sets of 20, 22, and 18 variables for ΔT_{res}, ΔT_{rec}, and $\Delta Loss_{max}$, respectively.

We compared four regression models, extreme gradient boosting (XGBoost), random forest (RF), multiple linear regression (MLR), and support vector regression (SVR), to predict each response-difference metric using its corresponding predictor

set. The data were randomly split into training (70%) and testing (30%) subsets. Hyperparameters were optimized via the Optuna framework combined with five-fold cross-validation on the training set, and early stopping (patience = 50 rounds) was applied as a regularization technique to prevent overfitting[80]. The tuned hyperparameter configurations were detailed in Supplementary Tab. 5. XGBoost consistently outperformed the other models across all three prediction tasks, achieving testing R^2 values of 0.800, 0.863, and 0.817 for ΔT_{res}, ΔT_{rec}, and $\Delta Loss_{max}$, respectively, with corresponding RMSE values of 0.11 months, 0.19 months, and 0.216×10^{-4} (Supplementary Fig. 16; Supplementary Tab. 6). Receiver operating characteristic (ROC) analysis further confirmed the robust discriminative ability of the XGBoost models, with area under the curve (AUC) values exceeding 0.85 for all three tasks, surpassing the suboptimal model (RF; Supplementary Fig. 17). Based on these performance advantages, we selected XGBoost as the final interpretable model.

To interpret the XGBoost model outputs and quantify the contributions of individual drivers, we applied the SHapley Additive exPlanations (SHAP) method. SHAP provides a unified framework for interpreting model predictions by decomposing each prediction into additive feature contributions, grounded in cooperative game theory[81]. Unlike conventional feature importance measures that rely on permutation or impurity-based metrics, SHAP satisfies desirable consistency and local accuracy properties, ensuring that the assigned importance values reliably reflect each feature's marginal contribution[82]. This approach has been widely employed in ecological attribution studies to reveal nonlinear driver–response relationships and threshold effects[81,83]. We computed SHAP values for all valid samples to ensure that the attribution results reflected the complete spectrum of environmental conditions. For each predictor, we calculated the mean absolute SHAP value across all samples as a measure of global importance. The relative contribution of each predictor to the model output was then quantified as:

$$Contribution_i = \frac{MeanAbs(SHAP)_i}{\sum_{i=1}^{p} MeanAbs\left(SHAP\right)_i} \times 100\% \quad (3)$$

Where $MeanAbs(SHAP)_i$ is the average of the absolute SHAP values for feature i across all samples, and p is the total number of predictors. A higher mean absolute SHAP value indicates a greater influence on the predicted response, and the contribution percentage reflects the proportion of total explained importance attributable to that feature. To examine the direction and nonlinearity of each driver's effect, we generated partial dependence plots by plotting predictor values against their corresponding SHAP values, with all other variables held at their observed values. Positive SHAP values indicate that the feature contributes positively to the model output (i.e., an increase in the response difference), whereas negative values indicate the opposite effect. This approach enabled us to identify critical thresholds and saturation points in the relationships between environmental drivers and vegetation response disparities[84].

Building on the six most influential drivers identified by XGBoost-SHAP (ranked by mean absolute SHAP value), we constructed partial least squares structural equation models (PLS-SEM) to disentangle their direct and indirect pathways influencing the divergent vegetation responses[59]. Separate PLS-SEMs were developed for ΔT_{res}, ΔT_{rec}, and $\Delta Loss_{max}$, with the six predictors incorporated as exogenous and mediating variables. All hypothesized paths were retained without pruning based on statistical significance. Path coefficients were estimated using the partial least squares algorithm with a path weighting scheme, and model fit was assessed using the goodness-of-fit index (GFI) and standardized root mean square residual (SRMR)[85]. All models demonstrated acceptable fit (GFI > 0.90, SRMR < 0.08; Supplementary Tab. 7). Standardized path coefficients were interpreted as direct effects, and total effects were calculated as the sum of direct and indirect effects. This complementary framework, combining XGBoost-SHAP for predictive attribution with PLS-SEM for

mechanistic path analysis, yielded a comprehensive understanding of the drivers and causal pathways underlying the divergent vegetation responses to SoilDH versus MetDH.

References

1. Fan, X., Zhang, Y., Shi, K., et al. Surging compound drought–heatwaves underrated in global soils [J]. *P. Natl. Acad. Sci. Usa*. **121(42)**, e2410294121 (2024).
2. Jiang, L., Zhang, J., Bai, L., et al. Increased frequency and severity of global compound dry and heat wave events in a daily scale. *J. Hydrol.* **654**, 132857 (2025).
3. Chen, D., Qiao, S., Yang, J. et al. Contribution of anthropogenic influence to the 2022-like Yangtze River valley compound heatwave and drought event. *Npj Clim. Atmos. Sci.* **7**, 172 (2024).
4. Tripathy, K. P., Mishra, A. K. How unusual is the 2022 European compound drought and heatwave event? *Geophys. Res. Lett*. **50**, e2023GL105453 (2023).
5. Van der Woude, A.M., Peters, W., Joetzjer, E. et al. Temperature extremes of 2022 reduced carbon uptake by forests in Europe. *Nat. Commun.* 14, 6218 (2023).
6. Yoon, D., Chen, J.H., Seo, E. Contribution of land-atmosphere coupling in 2022 CONUS compound drought-heatwave events and implications for forecasting. *Weather Clim. Extreme.* **46**, 100722 (2024).
7. Zhang, G., Zhang, S., Wang, H., et al. Evaluating vegetation vulnerability under compound dry and hot conditions using vine copula across global lands. *J. Hydrol.* **631**, 130775 (2024).
8. Yan, W., Zhou, J., Wang, X. et al. Vegetation resistance to compound drought and heatwave events buffers the spatial shift velocities of vegetation vulnerability. *Commun. Earth Environ.* **6**, 320 (2025).
9. Guan, H., Zhu, P., Huang, J., et al. Unraveling the Interplay: Intensive Solar Radiation Amplifies Maize Yield Reduction Under Dry-Heat Stress[J]. *Earth's Future.* **13(12)**, e2025EF006388 (2025).
10. Kong, M., Feng, Y., Lin, Z., et al. Divergent trends in global vegetation sensitivity to soil moisture and atmospheric dryness. *J. Hydrol.* **676**, 135721 (2026).
11. Bian, Y., Sun, P., Zhang, Q., et al. Amplification of non-stationary drought to heatwave duration and intensity in eastern China: Spatiotemporal pattern and causes. *J. Hydrol.* **612**, 128154 (2022).
12. Gu, L., Schumacher, D.L., Fischer, E.M., et al. Flash drought impacts on global ecosystems amplified by extreme heat. *Nat. Geosci.* **18**, 709-715 (2025).
13. Hao, Z., Hao, F., Xia, Y., et al. Compound droughts and hot extremes: Characteristics, drivers, changes, and impacts. *Earth-Sci. Rev.* **235**, 104241 (2022).
14. Liu, Z., Jiao, L., Lian, X. Impacts of increasing compound hot-dry events on vegetation under the warming-wetting trend in Northwest China. *Geography and Sustainability*. **6(2)**, 100222 (2025).
15. Huang S., Wang S., Wang C., et al. Soil moisture deficits amplify and prolong vegetation

productivity losses under compound dry-hot extremes. *The Innovation Geoscience*. **4**, 100235 (2026).
16. Liang, Y., Wang, J., Hao, Z. et al. Anthropogenically-driven escalating impact of soil-based compound dry-hot extremes on vegetation productivity. *Nat. Commun*. **17**, 2303 (2026).
17. Yao, Y., Fu, B., Liu, Y., et al. Compound hot-dry events greatly prolong the recovery time of dryland ecosystems [J]. *Natl Sci Rev*. **11(10)**, 274 (2024).
18. Yao, T., Wu, C., Yeh, P., et al. Widespread global enhancement of vegetation resistance to compound dry-hot events due to anthropogenic climate change. *Ecol. Indic*. **178**, 113880 (2025).
19. Shi, G., D. Wei, M. Qi, et al. Frequent Dry–Hot Extremes Slow the Loss of Semi-Arid Ecosystem Resilience. *Global Change Biol*. **32(4)**, e70835 (2026).
20. Chai, Y., Miao, C., AghaKouchak, A. et al. Flash droughts exacerbate global vegetation loss and delay recovery. *Nat. Commun*. **17**, 485 (2026).
21. Xu, X., Gui, X., Wu, G., et al. Assessment of vegetation vulnerability under compound drought-heat stress from an ecological engineering perspective in China. *Sci. China Earth Sci.* **69 (4)**: 1363–1386 (2026).
22. Wang, Y., Miao, C., Huntingford, C. et al. Compound atmospheric and soil droughts amplify the global loss of vegetation productivity. *Commun. Earth Environ*. (2026).
23. Huang, M., Zhai, P. Protracted vegetation recovery after compound drought and hot extreme compared to general drought. *Environ. Res. Lett*. **20**, 024001 (2025).
24. Novick, K., Ficklin, D., Stoy, P. et al. The increasing importance of atmospheric demand for ecosystem water and carbon fluxes. *Nat. Clim. Change*. **6**, 1023–1027 (2016).
25. Wang, M., Wang, Y., Liu, X., et al. Vapor pressure deficit dominates vegetation productivity during compound drought and heatwave events in China's arid and semi-arid regions: Evidence from multiple vegetation parameters. *Ecol. Inform.* **88**, 103144 (2025).
26. Li, X., Zhao, L., Zhang, T., et al. Assessing the impacts of dry-heat extremes on grassland gross primary productivity across mainland China using multi-source remote sensing data. *Information Geography.* **2(1)**, 100038 (2026).
27. Wu, T., Liu, Y., Chen, L. et al. Human pressure and biodiversity modify forest resilience after extreme multi-year droughts. *Nat. Ecol. Evol*. **10**, 880–892 (2026).
28. Gupta, A., Karthikeyan, L., Mishra, A., et al. Dominant role of soil moisture regulating vegetation water content during flash drought evolution. *Geophys. Res. Lett.* **53**, e2025GL119366 (2026).
29. Yao, Y., Liu, Y., Song, J., et al. Declining tradeoff between resistance and resilience of ecosystems to drought. *Earth's Future*. **12**, e2024EF004665 (2024).
30. Yuan, W., Zheng, Y., Piao, S., et al. Increased atmospheric vapor pressure deficit reduces global vegetation growth. *Sci. Adv*. **5(8)**, 1396 (2019).
31. Ding, Z., Peng, J., Qiu, S., et al. Nearly half of global vegetated area experienced inconsistent vegetation growth in terms of greenness, cover, and productivity. *Earth's Future.* **8**, e2020EF001618 (2020).
32. Jiang, F., Xie, X., Wang, Y., et al. Vegetation greening intensified transpiration but constrained soil evaporation on the Loess Plateau. *J. Hydrol.* **614**, 128514 (2022).

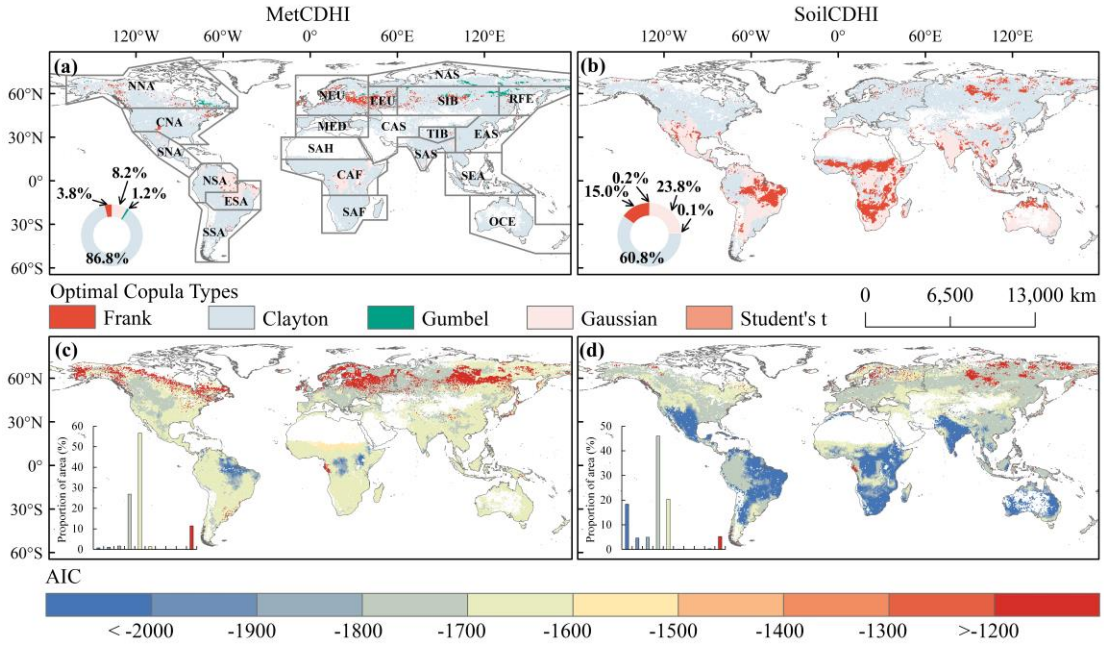
33. Li, Z., Sun, F., Wang, H., et al. Detecting the interactions between vegetation greenness and drought globally. *Atmos. Res*. **304**, 107409 (2024).
34. Liu, Y., Li, Z., Chen, Y., et al. Global greening drives significant soil moisture loss. Commun. *Earth Environ*. **6**, 601–614 (2025).
35. Huang, M., Lu, R., Zhou, Y. Divergent responses of canopy structure and productivity to drought and their driving mechanisms in northern China's grasslands. *Agr. Water Manage.* **329**, 110364 (2026).
36. Liu, Q., Wu, C., Gao, L., et al. Coordination between non-structure carbohydrates and hydraulic function under different drought duration, intensity, and post-drought recovery. *Environ. Exp. Bot.* **215**, 105485 (2023).
37. Jiang, P., Meinzer, F. C., Wang, H., et al. Spatio-temporal variation in deep soil water use patterns of overstorey and understorey layers in subtropical plantations predicts community assembly. *J. Ecol.* **110**, 2998–3011 (2022).
38. Liu, Z., Ye, L., Jiang, J., et al. Increased uptake of deep soil water promotes drought resistance in mixed forests. *Plant, Cell & Environment.* **46**, 3218–3228 (2023).
39. Jiang, C., Tetzlaff, D., Wu, S., et al. Exploring impacts of forest management strategies on water partitioning in a drought-sensitive catchment using a tracer-aided ecohydrological framework. *Hydrol. Earth Syst. Sc.* **30**, 3715–3739 (2026).
40. Yu, H., Zhu, L., He, X., et al. Resistance, Resilience, and Recovery Time of Grasslands in Response to Different Drought Patterns. *Remote Sens-basel.* **17(3)**, 559 (2025).
41. Shi, Q., Montgomer, D.R., Swann, A.L.S., et al. Agroseismology and the impact of farming practices on soil hydrodynamics. *Science*. **392(6795)**, 306-310 (2026).
42. Zhu, X., Wang, L., Shi, L., et al. Ecological drought is globally driven by soil characteristics rather than climate aridity. *J. Hydrol.* **653**, 132799 (2025).
43. King, A. E., E. Choi, J. Burkhardt, et al. Soil Organic Carbon Improves Crop Yield and Yield Resilience. *Global Change Biol.* **32(5)**, e70909 (2026).
44. Liu, J., Wang, O., Zhan, W., et al. When and where soil dryness matters to ecosystem photosynthesis. *Nat. Plants.* **11**, 1390-1400 (2025).
45. Bai, Y., Tang, Z. Enhanced effects of species richness on resistance and resilience of global tree growth to prolonged drought. *PNAS.* **121(39)**, e2410467121 (2024).
46. Wang, H., Maestre, F.T., Lu, N. et al. Persistence and turnover of soil organic carbon in global drylands. *Nat. Commun.* **17**, 3565 (2026).
47. Cao, M., Wang, W., Wei, J., et al. Revegetation impacts on moisture recycling and precipitation trends in the Chinese Loess Plateau. *Water Resour. Res.* **60**, e2024WR038199 (2024).
48. He, M., K. E. Barry, E. T. Borer, et al. Prolonged Nutrient Enrichment Slows the Recovery of Biodiversity and Productivity After Its Cessation. *Global Change Biol*. **32(7)**, e70981 (2026).
49. Hong, Y., Petrie, M.D., Zhang, Y. et al. Widespread controls of precipitation sensitivity on drought recovery of global forests. *Nat. Commun*. (2026).
50. Deng, J., Duan, Y., Ma, Z., et al. Regional compound drought and heatwave events over China and evaluation of ERA5-Land dataset based on classification approach. *Weather Clim. Extreme*. **52**, 100874 (2026).

51. Miao, C., Zhang, Q., Li, X., et al. Global drought extremes in 2025. *Nat. Rev. Earth Env*. **7**, 277-279 (2026).
52. Wieder, W.R., J. Boehnert, et al. Regridded Harmonized World Soil Database v1.2. Data set. Available on-line [http://daac.ornl.gov] from Oak Ridge National Laboratory Distributed Active Archive Center, Oak Ridge, Tennessee, USA, (2014).
53. Wankmüller, F.J.P., Delval, L., Lehmann, P. et al. Global influence of soil texture on ecosystem water limitation. *Nature*. **635**, 631–638 (2024).
54. Li, M., Cao, S., Zhu, Z., et al. Spatiotemporally consistent global dataset of the GIMMS Normalized Difference Vegetation Index (PKU GIMMS NDVI) from 1982 to 2022. *Earth Syst. Sci. Data.* **15**, 4181–4203 (2023).
55. Liu, Y., Zhang, Z., Tong, L., Khalifa, M., Wang, Q., Gang, C., et al. Assessing the effects of climate variation and human activities on grassland degradation and restoration across the globe. *Ecol. Indic.* **106**, 105504 (2019).
56. Liu, L., Cao, X., Li, S. et al. A 31-year (1990–2020) global gridded population dataset generated by cluster analysis and statistical learning. *Sci. Data*. **11**, 124 (2024).
57. Kummu, M., Kosonen, M. Masoumzadeh Sayyar, S. Downscaled gridded global dataset for gross domestic product (GDP) per capita PPP over 1990–2022. *Sci. Data*. **12**, 178 (2025).
58. Cheng, H., Geng, M., Li, X., et al. A temporally consistent global 500 m-resolution monthly VIIRS-like nighttime light dataset (1992-2024). *Earth Syst. Sci. Data*. **18**, 3449–3479 (2026).
59. Theobald, D.M., Oakleaf, J.R., Moncrieff, G. et al. Global extent and change in human modification of terrestrial ecosystems from 1990 to 2022. *Sci. Data*. **12**, 606 (2025).
60. Ma, Z., Chen, D., Sun, P., et al. Actual evapotranspiration dominated net primary productivity loss caused by concurrent droughts. Ecol. Indic. 176, 113645 (2025).
61. Huang, J., Yu, H., Guan, X. et al. Accelerated dryland expansion under climate change. *Nat. Clim. Change*. **6**, 166–171 (2016).
62. Iturbide, M., Gutiérrez, J.M., Alves, L.M., et al. An update of IPCC climate reference regions for subcontinental analysis of climate model data: deffnition and aggregated datasets. *Earth Syst. Sci. Data*. **12(4)**, 2959–2970 (2020).
63. McKee, T.B.; Doesken, N.J.; Kleist, J. The Relationship of Drought Frequency and Duration to Time Scales. In Proceedings of the 8th Conference on Applied Climatology, Anaheim, CA, USA, 17–22 January (1993).
64. Su, Y., Wang, W., Zhao, W., et al. Higher vulnerability but faster recovery in planted than natural forests during the 2022 compound drought–heatwave in China's Yangtze River Basin. *Water Resour. Res*. **62**, e2026WR044482 (2026).
65. Mei, L., Aru, H., Tong, S., et al. Study on the propagation processes and driving mechanisms of meteorological, hydrological, and agricultural droughts on the Mongolian Plateau. *J. Hydrol.* **660**, 133511 (2025).
66. Kong, Y., Guo, E., Wang, T., et al. Response of gross primary productivity to compound dry and hot events in Inner Mongolia under large-scale circulation patterns. *Global Planet. Change.* **260**, 105392 (2026).
67. Li, J., Bevacqua, E., Wang, Z. et al. Hydroclimatic extremes contribute to asymmetric trends in ecosystem productivity loss. *Commun. Earth Environ*. **4**, 197 (2023).

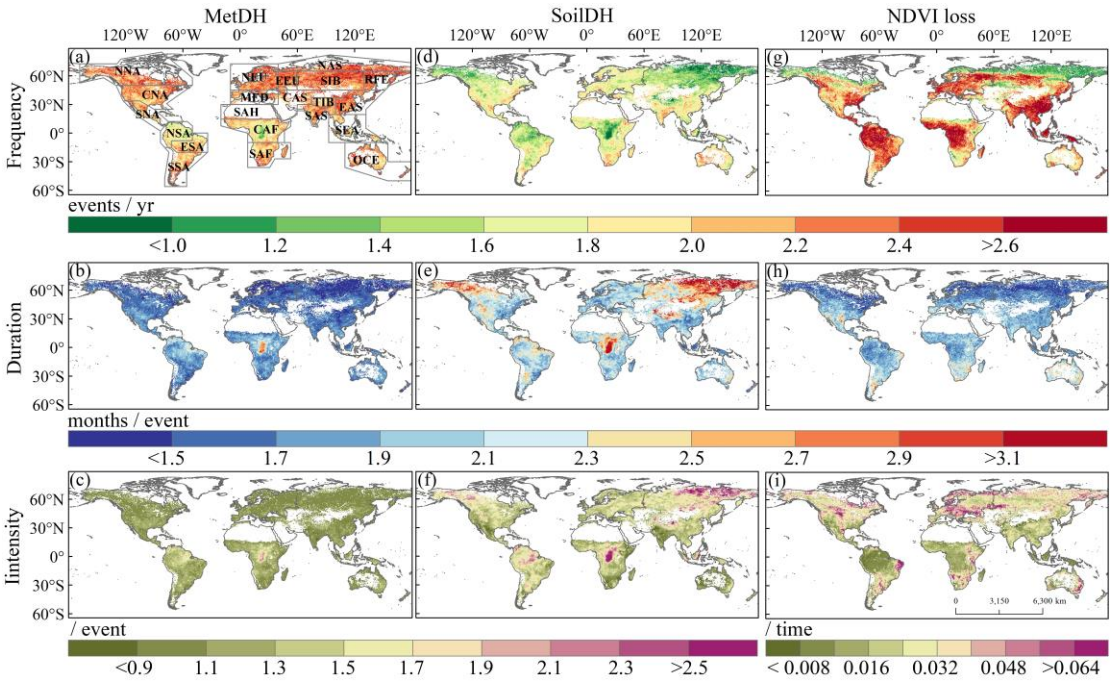
68. Black, E., Wainwright, C., Allan, R.P. et al. Emerging hotspots of agricultural drought under climate change. *Nat Geosci.* **19**, 303–310 (2026).
69. Cao, S., Li, L., He, C., et al. Standardized compound drought and heatwave index: A new compound drought and heatwave events monitoring index considering evapotranspiration effects. *Int. J. Appl. Earth. Obs*. **146**, 105023 (2026).
70. Cleveland, R. B., Cleveland, W. S., McRae, J. E., et al. STL: A seasonal-trend decomposition procedure based on loess. *J. Off. Stat*. **6(1)**, 3–73 (1990).
71. Wu, J., Zhao, Q., Zhou, Y, et al. Temperature and water availability drive vegetation resilience dynamics in China: An empirical study from causal perspective. *J. Geogr. Sci.* **35(10)**, 2069-2090 (2025).
72. Fu, L., Huang, J., Li, C. et al. Critical slowing down of semiarid vegetation resilience is amplified by intensifying heatwaves. *Nat. Commun*. (2026).
73. Dong, Y. X., Liu, G. M., Wu, X. D., et al. Spatiotemporal Variations in Compound Extreme Events and Their Cumulative and Lagged Effects on Vegetation in the Northern Permafrost Regions from 1982 to 2022. *Remote sens-basel*. **17(1)**, 169 (2025).
74. Xing, Y., Wang, S., Wang, A., et al. Spatiotemporal dynamics of meteorological and groundwater droughts in Southwest China and their cumulative and lagged impacts on vegetation. *J. Hydrol*. 135086 (2026).
75. Yuan, B., Guo, S., Zhang, X., et al. Quantifying the drought sensitivity of vegetation types in northern China from 1982 to 2022. *Agr. Forest Meteorol.* **359**, 110293 (2024).
76. Zhang, L., Jia, X., Zhao, Y. H., et al. Lagged and cumulative effects of drought on global vegetation greenness, coverage, and productivity. *Environ. Impact Asses*. **115**, 108019 (2025).
77. Wang, Y., Zhou, R., Xiao, J., et al. Cumulative and Legacy Effects of Droughts on Global Photosynthetic Phenology. *Phenology: An Integrative Environmental Science*. 531-551 (2024).
78. Liu, C., Shi, J., Wang, F., et al. Development and validation of an interpretable multi-task model to predict outcomes in patients with rhabdomyolysis: a multicenter retrospective cohort study. *EclinicalMedicine.* **87**, 103438 (2025).
79. Shi, H., Zhang, S., Li, M., et al. Understanding industrial land allocation in rural regions of China: spatiotemporal patterns and driving mechanisms. *Habitat Int.* **165**, 103574 (2025).
80. Diao, B., Shi, S., Li, J., et al. Machine Learning-Assisted Design and Discovery of High-Performance Cyanine-Based Photosensitizers for Integrated Theranostic Applications. *Adv. Mater*. **38(7)**, e15813 (2026).
81. Wang, W., Liu, S., Zhang, Q., et al. Increasing aridity and interannual precipitation variability drives resilience declines in restored forests across China. *Earth's Future*. **13**, e2025EF006164 (2025).
82. Lundberg, S. M., & Lee, S.-I. A Unified Approach to Interpreting Model Predictions. *NIPS*. **30**, 4765–4774 (2017).
83. Ren, Z., Li, C., Fu, B., et al. Effects of aridification on soil total carbon pools in China's drylands. *Global Change Biol.* **30(1)**, e17091 (2024).
84. Lu, J., Liu, X., Zhu, D., et al. Unveiling multiscale and nonlinear effects of land use change drivers through interpretable machine learning model: Insights from “Ecological-cost and

762 Economic-benefit" trade-off perspective. *Environ. Impact Asses*. **118**, 108254 (2026).
763 85. Hou, D., Jia, X., Wang, L., et al. ,Global soil pollution by toxic metals threatens agriculture
764 and human health. *Science*. **388**, 316-321 (2025).

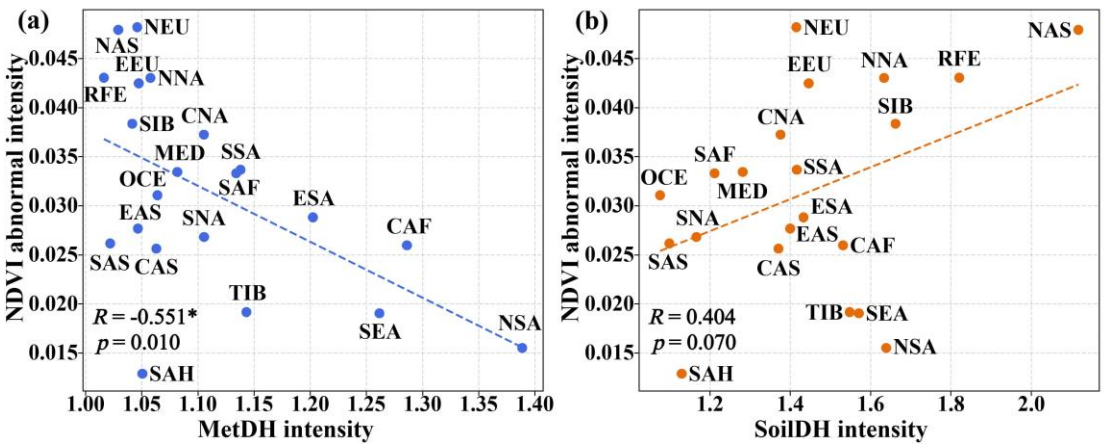
Supplementary Material



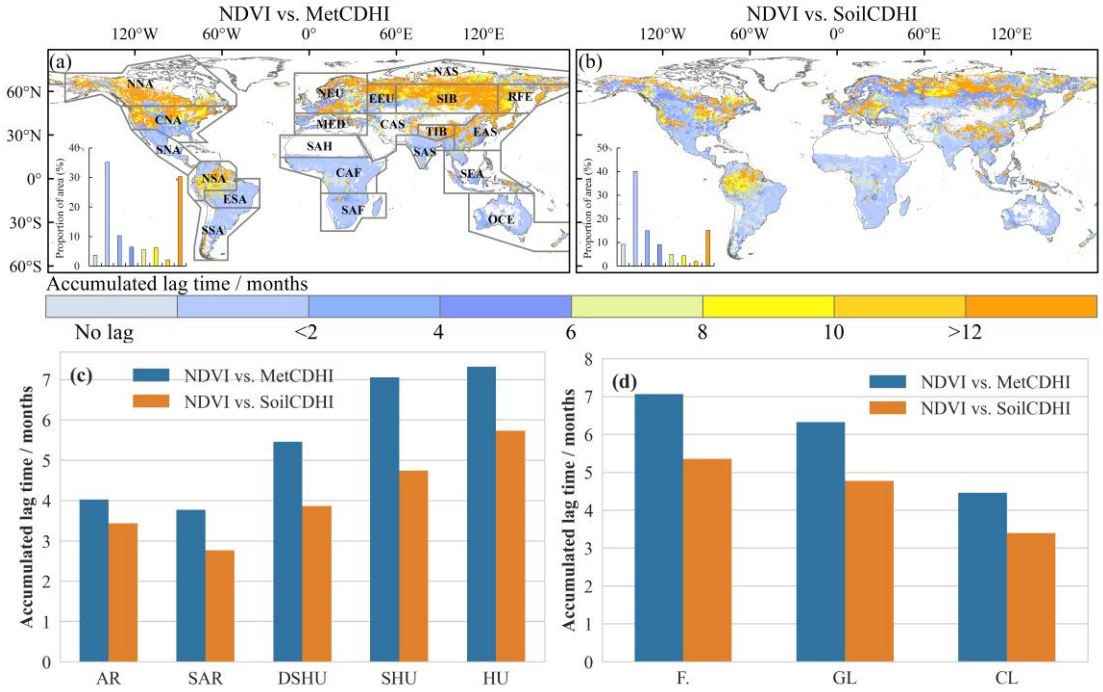
Supplementary Fig. 1 | Global distributions of optimal Copula families and AIC diagnostics. a, b, Spatial patterns of optimal Copula families for MetCDHI and SoilCDHI, respectively. Inset pie charts indicate the areal proportion of each Copula family (Frank, Clayton, Gumbel, Gaussian, Student's t). **c, d,** Corresponding spatial patterns of Akaike Information Criterion (AIC) values. Inset bar charts show the proportion of pixels within different AIC intervals. IPCC AR6 reference regions are shown in **a**.



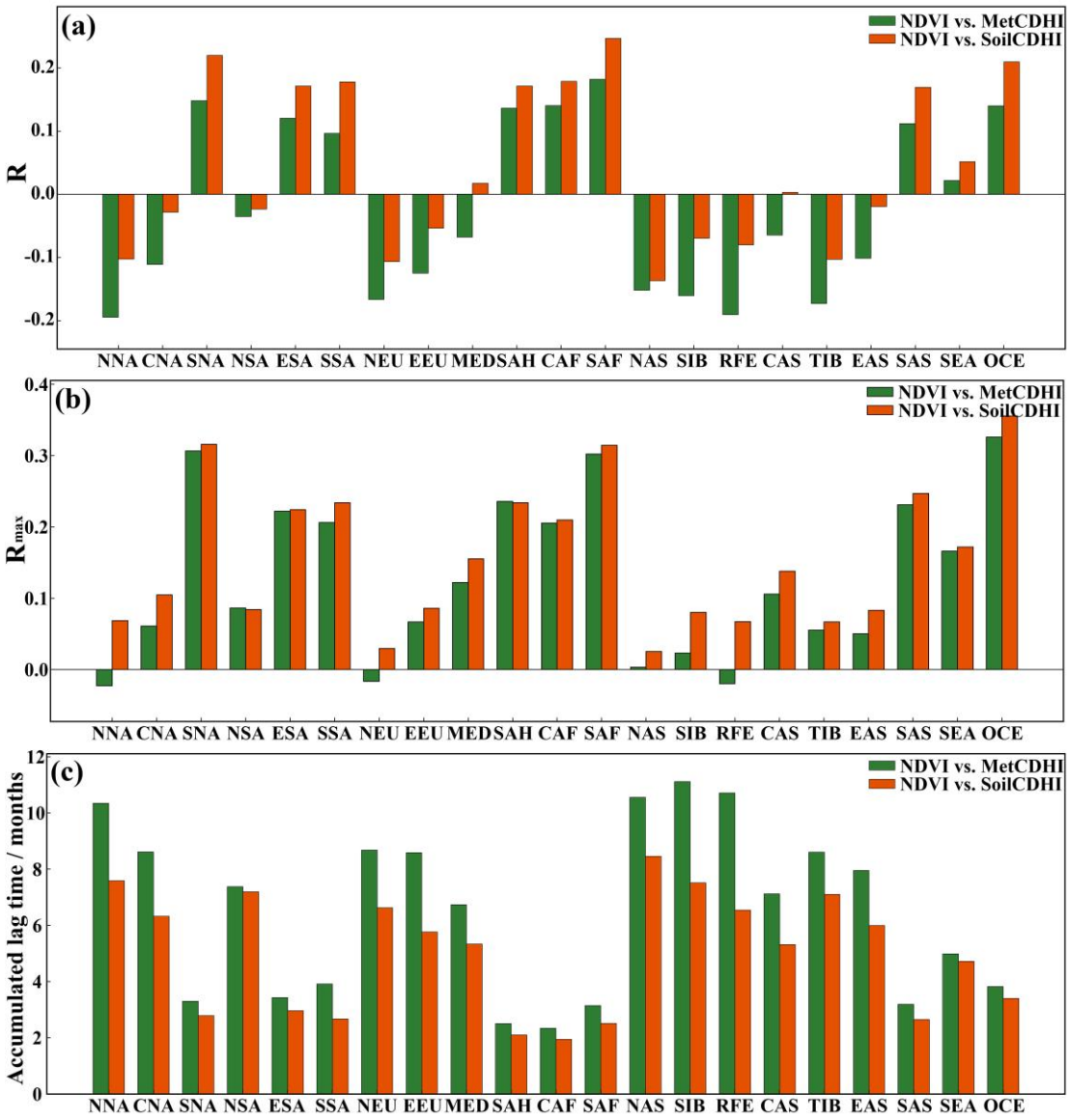
Supplementary Fig. 2 | Global spatial patterns of MetDH, SoilDH and NDVI loss during 1982-2022. a–c, Illustrate the frequency, duration, and intensity of MetDH. d-f, Illustrate the same three metrics for SoilDH. (g–i) show the frequency, duration, and intensity of NDVI loss. The grid boxes in panel a denote the boundaries of the 21 IPCC AR6 reference regions.



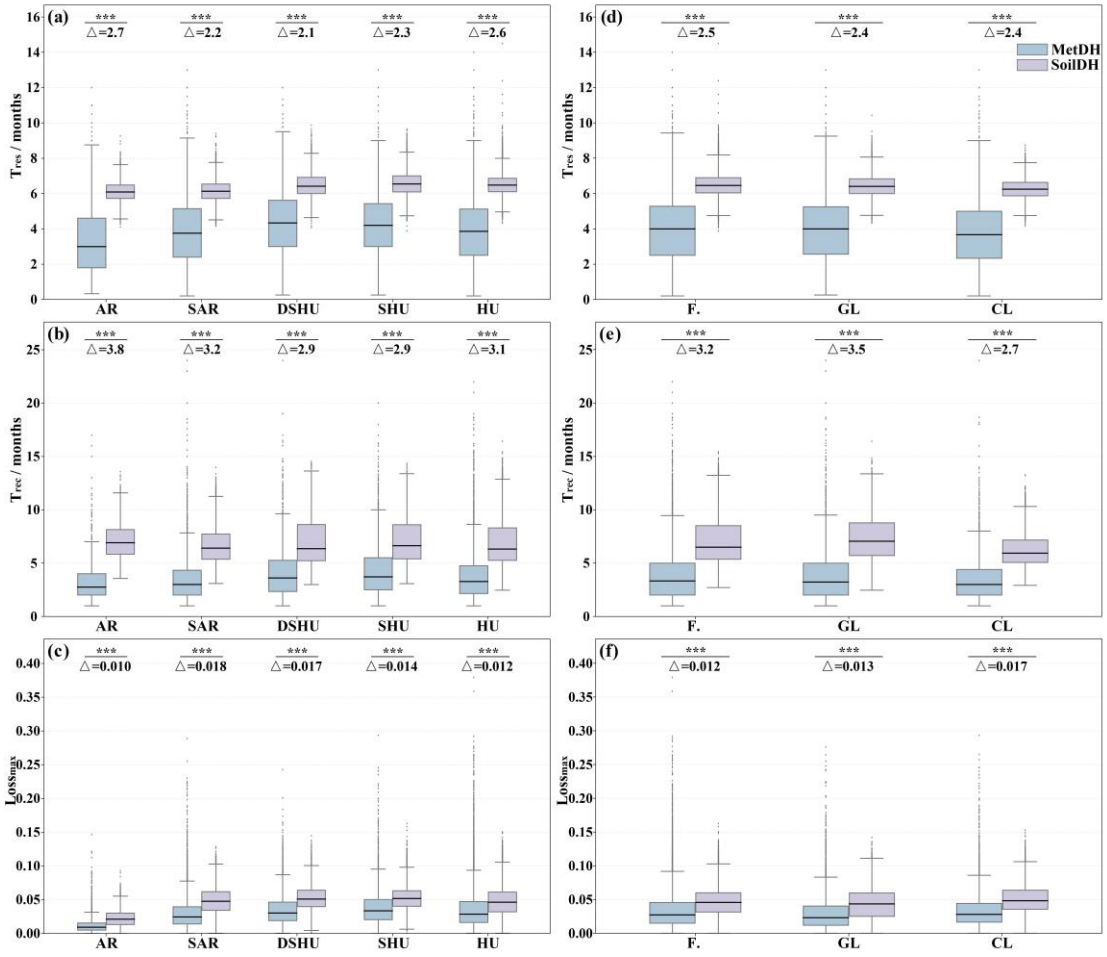
Supplementary Fig. 3 | Contrasting regional correlations between NDVI anomalies and CDHE intensities. a, b, Scatterplots showing the relationship between NDVI anomaly and MetDH **(a)** and SoilDH **(b)** intensities across the IPCC AR6 reference regions. Dashed lines represent linear regression fits.



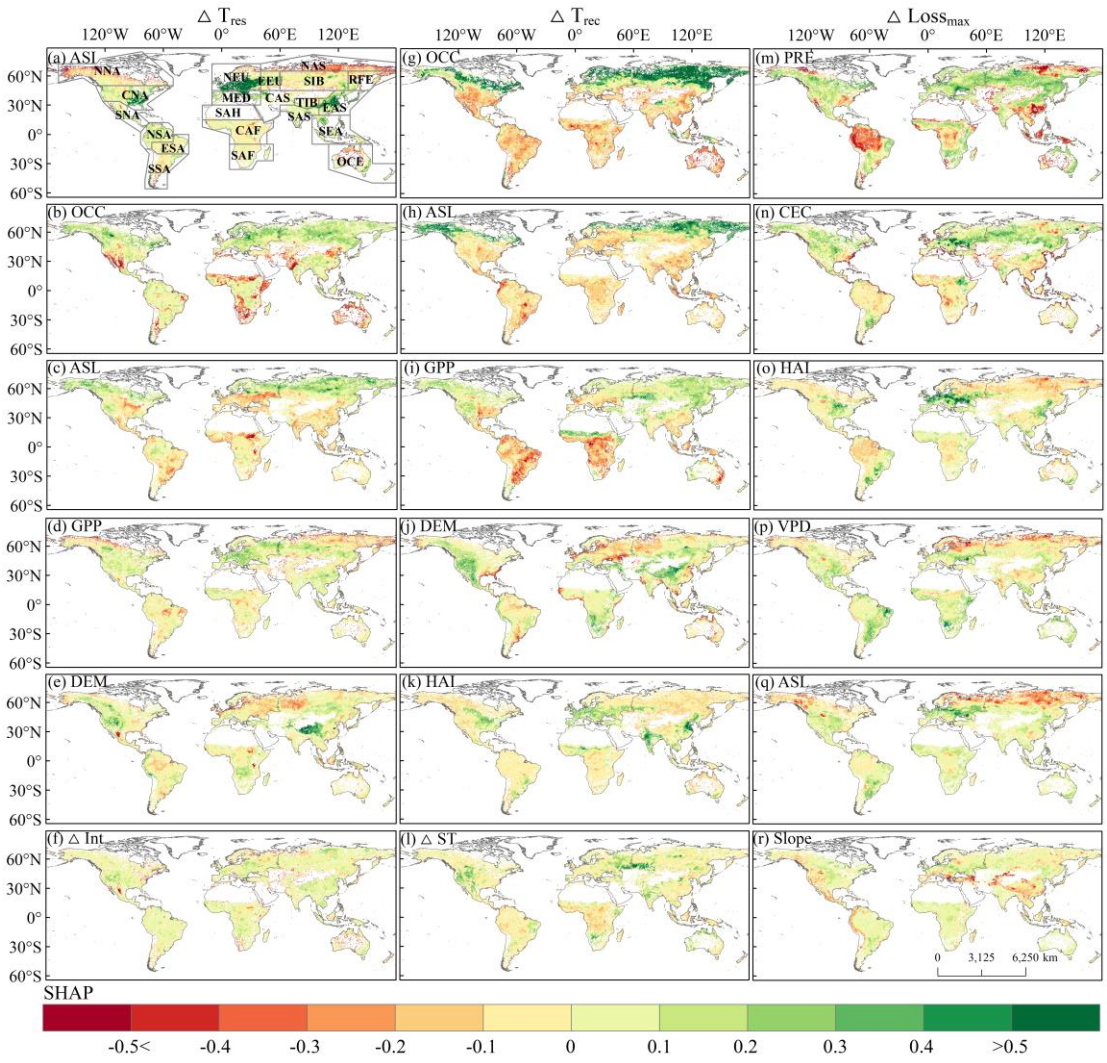
Supplementary Fig. 4 | Accumulated lag times of MetDH and SoilDH on global vegetation. a, b, Spatial patterns of the optimal accumulated lag time (months) for MetCDHI **(a)** and SoilCDHI **(b). c, d,** Summary statistics of the accumulated lag time across different climate zones **(c)** and vegetation functional types **(d).** IPCC AR6 regions are indicated in **a.**



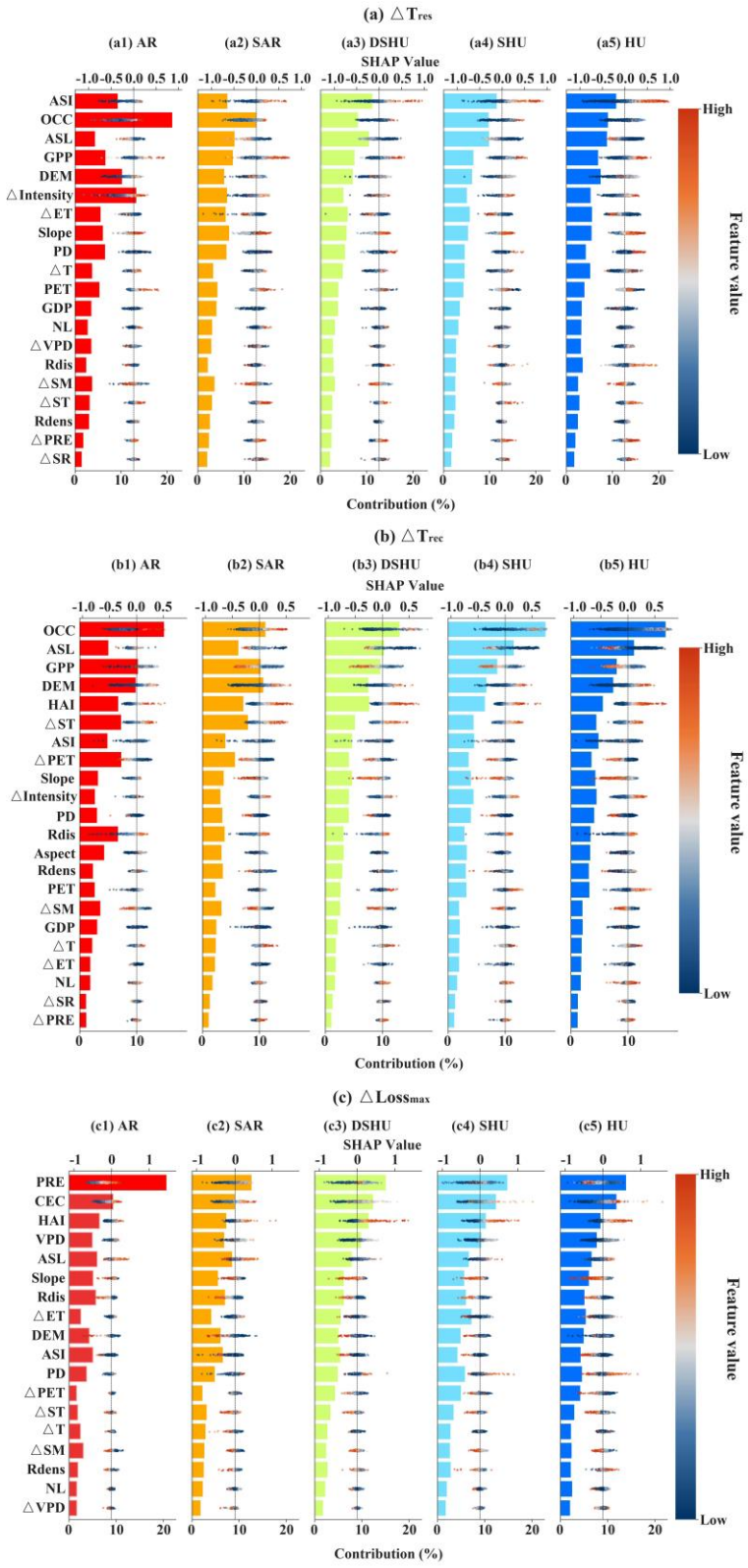
Supplementary Fig. 5 | Regional divergence in vegetation sensitivity to MetDH and SoilDH under cumulative effects. a, Mean contemporaneous correlations (R) between NDVI and MetCDHI and SoilCDHI across 21 IPCC AR6 regions. **b,** Mean maximum correlations (R_{max}) considering cumulative effects. **c,** Mean accumulated lag time (months) for each region.



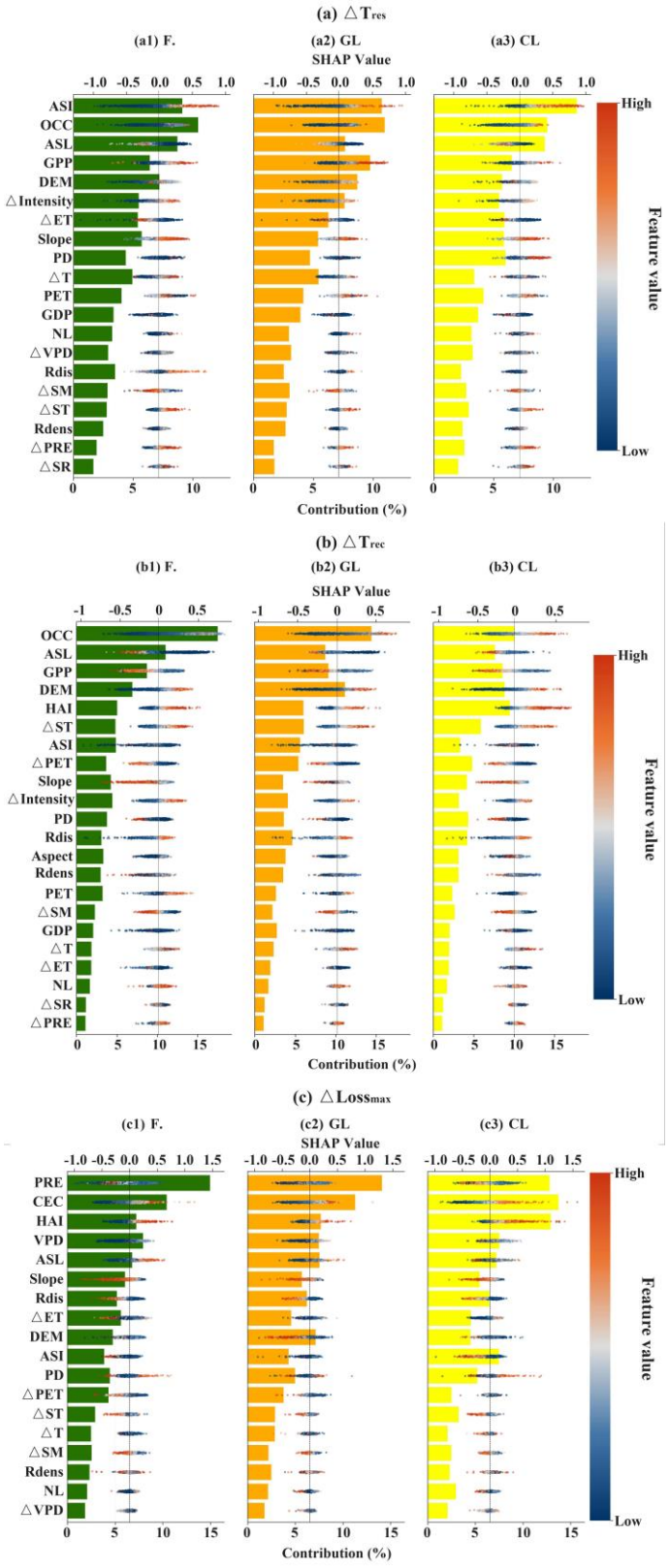
Supplementary Fig. 6 | Divergent response trajectories between SoilDH and MetDH across climate zones and vegetation functional types. a–c, Comparisons of resistance time (T_{res}), recovery time (T_{rec}), and maximum loss ($Loss_{max}$) for MetDH, SoilDH, and their differences (Δ) across climate zones. **d–f,** Same as **a–c,** but across vegetation functional types. The significance of differences between the two drought-hot indices within each category is indicated above the brackets (*** $p < 0.001$), based on the two-sided Mann-Whitney U test. The Δ values listed above the brackets represent the mean differences between the two drought-hot indices.



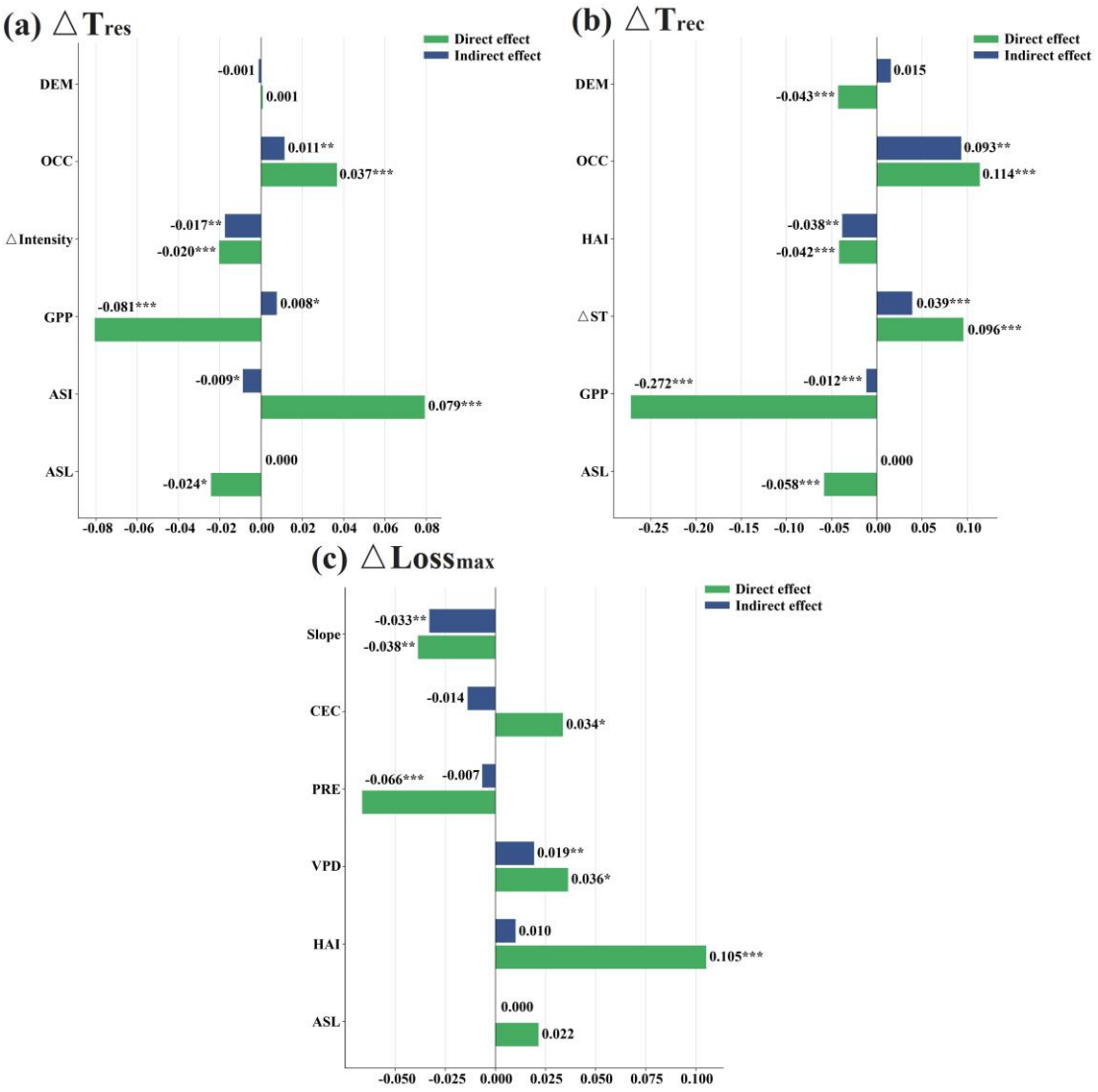
Supplementary Fig. 7 | Spatial distribution pattern of SHAP values for the six dominant predictors across theΔT_{res}, ΔT_{rec}, and $\Delta Loss_{max}$. a-f, Show the SHAP value distributions for the six most influential predictors on ΔT_{res}, namely ASI, OCC, ASL, GPP, DEM, and ΔIntensity. **g-l,** Display these for ΔT_{rec}, including OCC, ASI, GPP, DEM, HAI, and ΔST. **m-r,** Present the patterns for $\Delta Loss_{max}$, including PRE, CEC, HAI, VPD, ASL, and Slope. Positive and negative SHAP values indicate enhancing and suppressing local effects, respectively. The map in panel a displays the boundaries of the 21 IPCC AR6 reference regions.



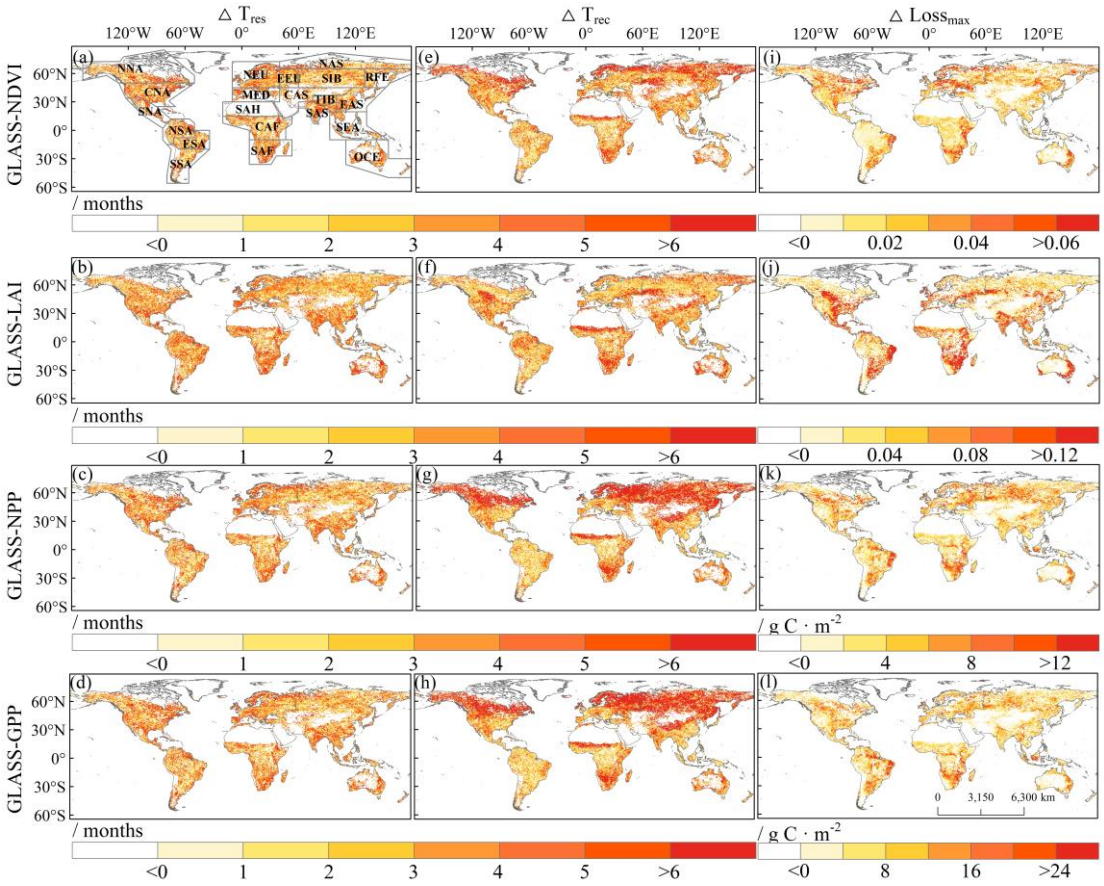
Supplementary Fig. 8 | SHAP-based feature attribution across climate zones. Feature importance and SHAP value distributions for ΔT_{res} **(a1–a5)**, ΔT_{rec} **(b1–b5)**, and $\Delta Loss_{max}$ **(c1–c5)** predicted by the XGBoost model across the arid, semi-arid, dry sub-humid, sub-humid, and humid climate zones. Bar lengths denote mean absolute SHAP importance, and colour gradients show feature magnitude.



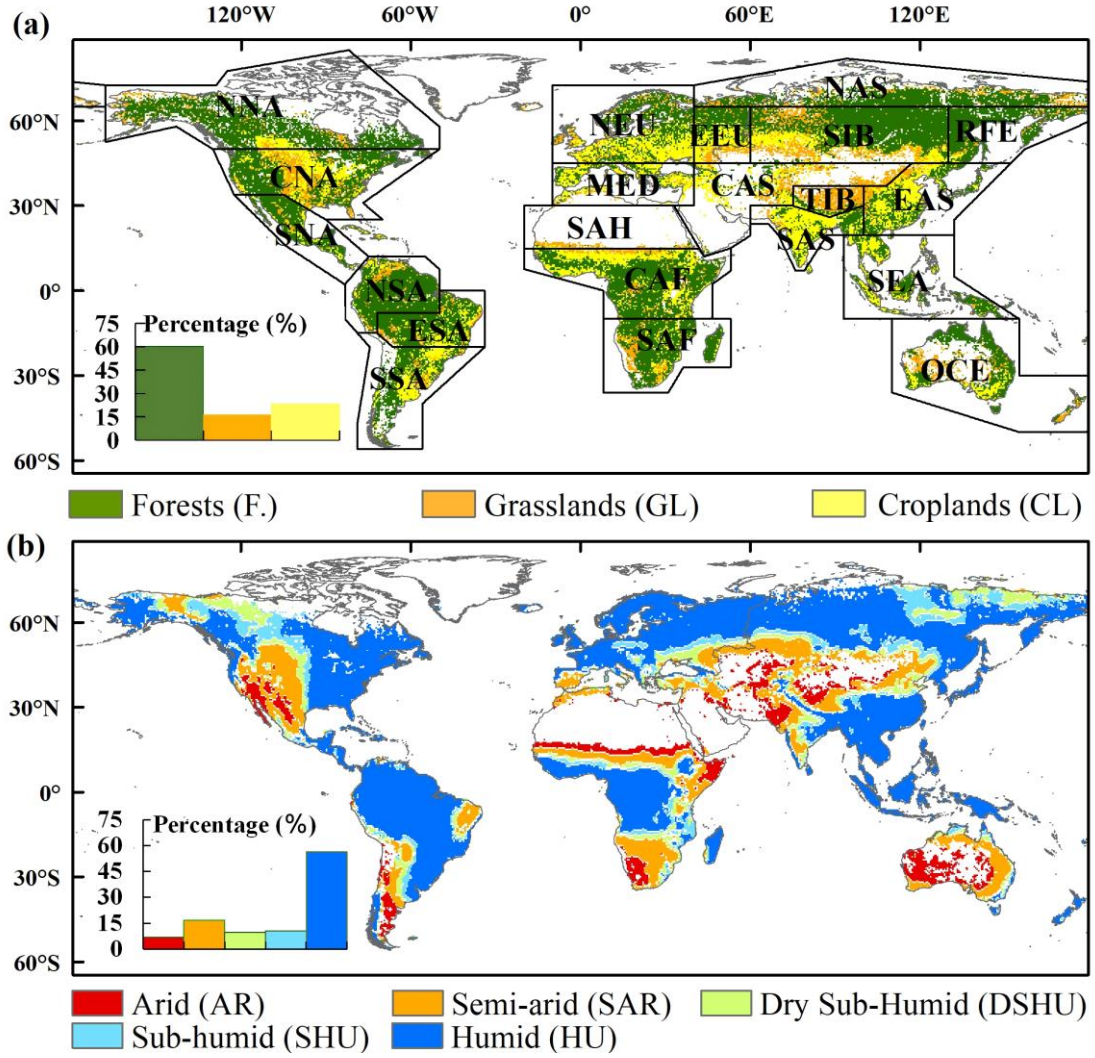
Supplementary Fig. 9 | SHAP-based feature attribution across vegetation functional types. Feature importance and SHAP value distributions for ΔT_{res} (a1–a3), ΔT_{rec} (b1–b3), and $\Delta Loss_{max}$ (c1–c3) predicted by the XGBoost model across the forest, grassland and cropland. Bar lengths denote mean absolute SHAP importance, and colour gradients show feature magnitude.



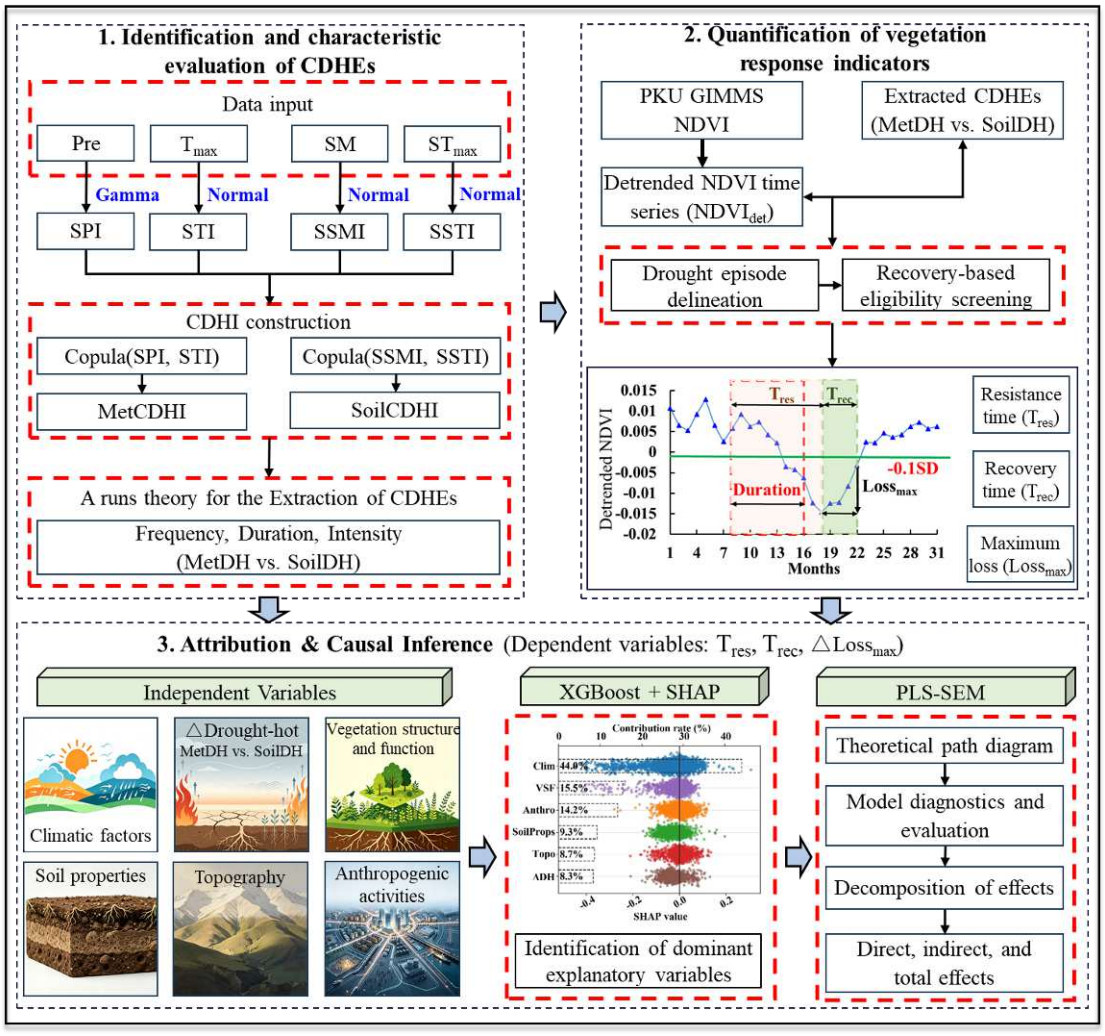
Supplementary Fig. 10 | Direct and indirect effects of driving factors on response differences. a–c, Bar charts decomposing the direct (green) and indirect (blue) standardized effects derived from PLS-SEM for ΔT_{res} **(a)**, ΔT_{rec} **(b)**, and $\Delta Loss_{max}$ **(c)**. Numbers adjacent to the bars indicate standardized path coefficients. Asterisks indicate statistical significance: *p < 0.05, **p < 0.01, ***p < 0.001.



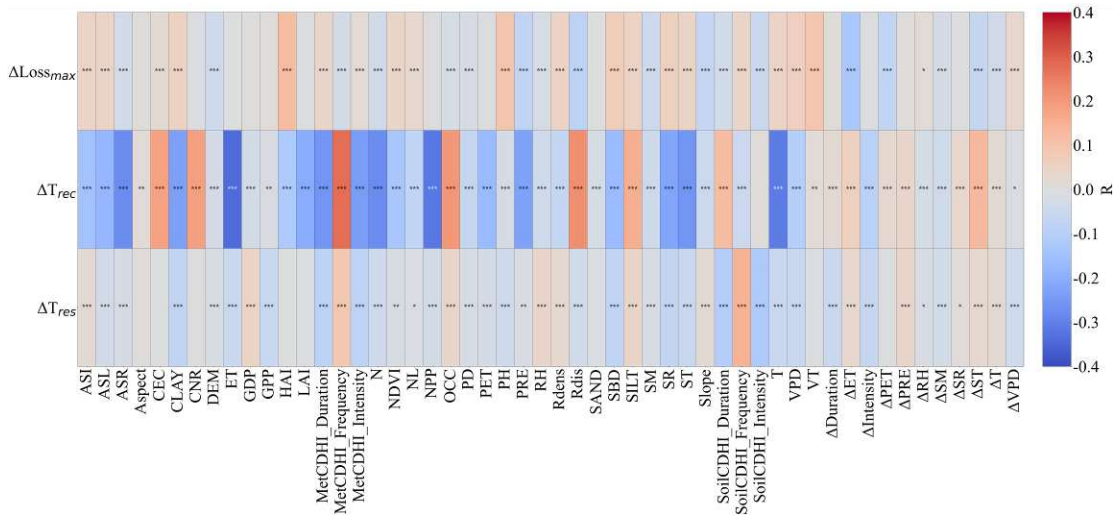
Supplementary Fig. 11 | Validation of response differences using GLASS vegetation proxies. a–c, Spatial patterns of ΔT_{res}, ΔT_{rec}, and $\Delta Loss_{max}$ derived from GLASS-NDVI. **d–f,** Same as **a–c,** but for GLASS-LAI. **g–i,** Same as **a–c,** but for GLASS-NPP. **j–l,** Same as **a–c,** but for GLASS-GPP. IPCC AR6 boundaries are shown in **a**.



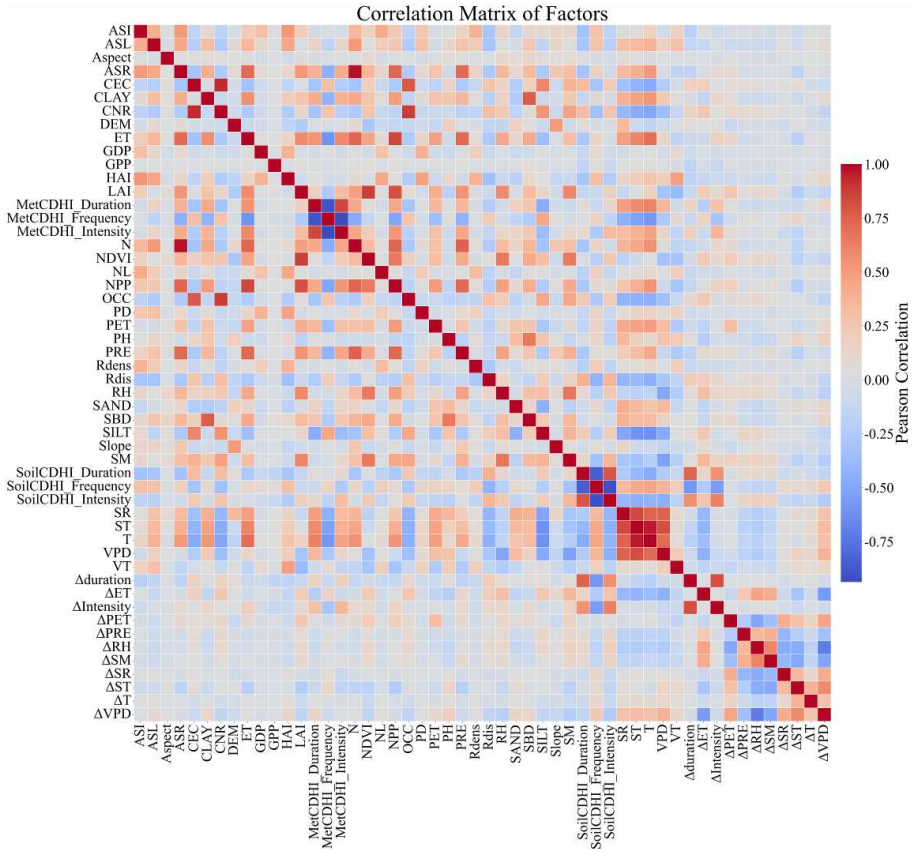
Supplementary Fig. 12 | Classification of global vegetation functional types and climate zones. a, Spatial distribution of stable vegetation functional zones across IPCC AR6 reference regions. **b,** Global spatial pattern of climate zones based on the aridity index for 1982–2022 (AR, arid; SAR, semi-arid; DSHU, dry sub-humid; SHU, sub-humid; HU, humid). Inset bar charts display the areal proportion of each class.



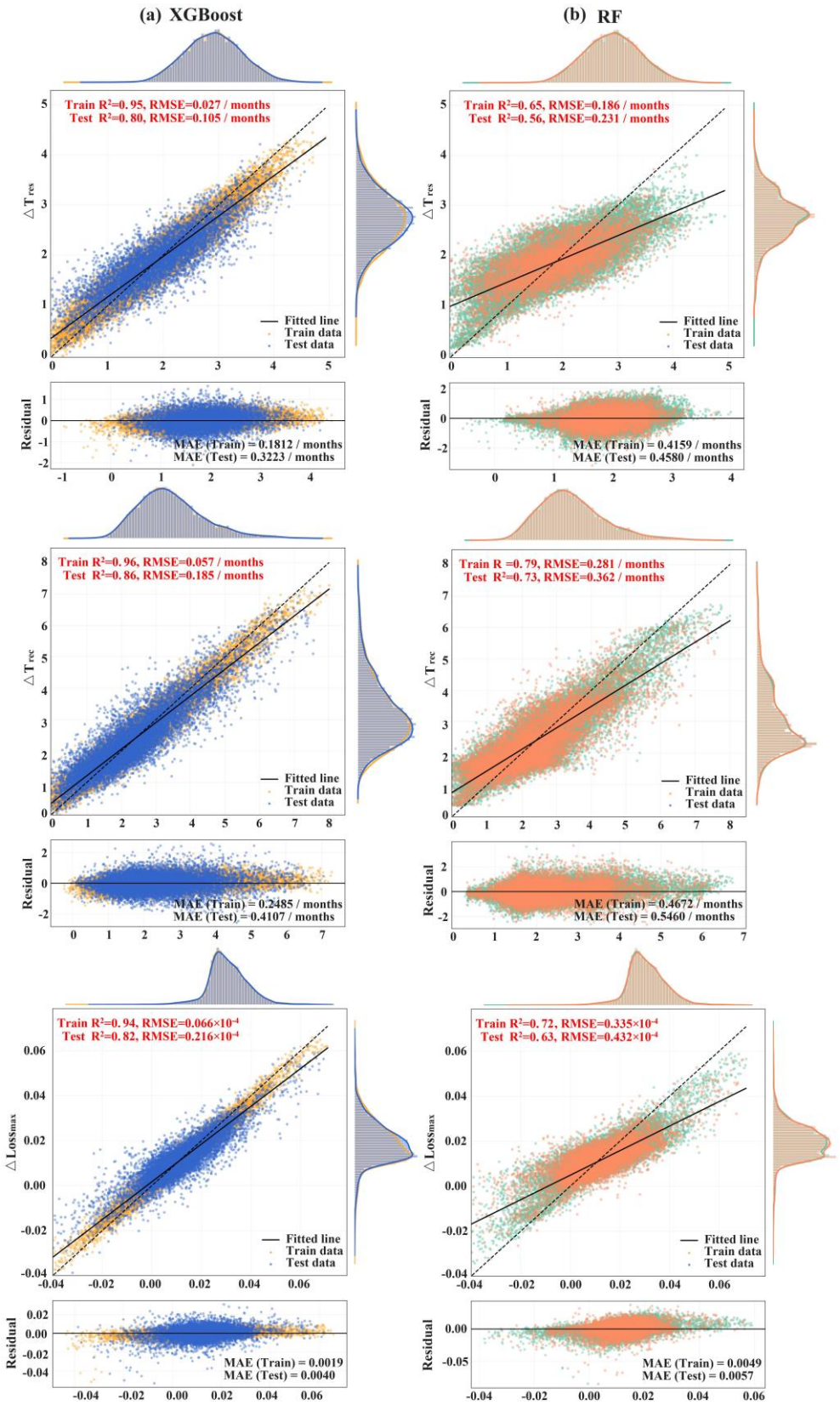
Supplementary Fig. 13 | Methodological framework of this study. Schematic overview illustrating the data inputs, index construction, CDHE event extraction, vegetation response trajectory quantification, and the two-step attribution analysis using XGBoost-SHAP and PLS-SEM.



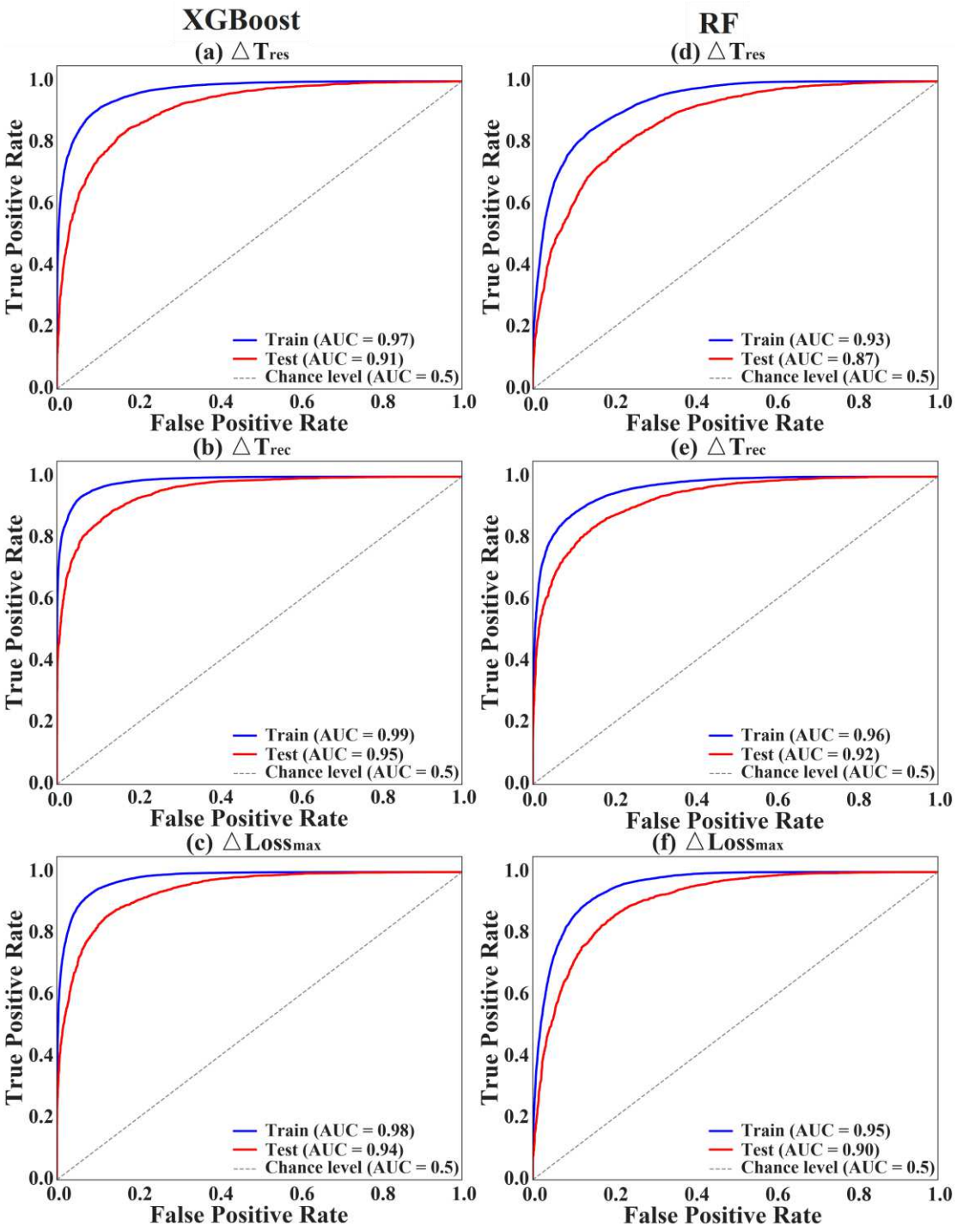
Supplementary Fig. 14 | Pearson correlation matrix between candidate predictors and response metrics. Correlations between 52 candidate drivers and the three response-difference metrics (ΔT_{res}, ΔT_{rec}, $\Delta Loss_{max}$). Asterisks indicate significance levels: *p < 0.05, **p < 0.01, ***p < 0.001. Predictors with *p < 0.05 were retained for subsequent modeling. Abbreviations of the driver variables are defined in Supplementary Table 3.



Supplementary Fig. 15 | Pairwise correlation heatmap of candidate predictors for multicollinearity screening. The colour-coded matrix displays Pearson correlation coefficients among all candidate drivers considered for the attribution analysis. The color scale ranges from dark blue (strong negative correlation) to dark red (strong positive correlation), with lighter colors indicating weaker correlations. The diagonal represents the self-correlation of each variable (R = 1.0). During the variable screening procedure, predictor pairs with an absolute correlation coefficient exceeding the threshold of $|R| > 0.6$ were regarded as highly collinear and were subjected to iterative removal (see also Methods and Supplementary Table 3).



Supplementary Fig. 16 | Training and test performance (R^2, RMSE and MAE) of the XGBoost and RF models for predicting response-difference metrics (SoilDH vs. MetDH). a–c, XGBoost performance for ΔT_{res}, ΔT_{rec} and $\Delta Loss_{max}$, respectively. **d–f,** Random Forest (RF) performance for ΔT_{res}, ΔT_{rec} and $\Delta Loss_{max}$, respectively. Training and test sets are shown alongside residual errors for reference.



Supplementary Fig. 17 | Receiver operating characteristic (ROC) curves for model performance. a–c, ROC curves for the XGBoost models predicting ΔT_{res}, ΔT_{rec}, and $\Delta Loss_{max}$, respectively. **d–f,** Same as **a–c,** but for the Random Forest (RF) models. Blue and red lines indicate training and testing sets, respectively. The dashed grey line denotes chance level (AUC = 0.5). Area under the curve (AUC) values are reported in the legends.

Supplementary Tab. 1 Detailed information on the dataset used in this study.

Category	Dataset	Variables	Native Resolution	Temporal Coverage	Application
Meteorological & Hydrological	ERA5-Land	PRE, T, T_{max}, T_d, SR, ET, PET, RH and VPD	0.1° × 0.1°, hourly	1982–2022	MetCDHI construction (PRE, T_{max}); AI calculation (PRE, PET); attribution analysis (PRE, T, SR, ET, PET, RH and VPD)
Soil	ERA5-Land	SM, ST, and ST_{max}	0.1° × 0.1°, hourly	1982–2022	SoilCDHI construction (SM, ST_{max}); attribution analysis (SM, ST)
	HWSD v1.2	SBD, SAND, SILT, CLAY, PH, CEC, OCC and CNR	1 km	Static covariates	Attribution analysis
Vegetation	PKU GIMMS NDVI	NDVI	1/12°, 15-day	1982–2022	Response metric extraction
	GLASS	NDVI, LAI, GPP and NPP	0.05°, 8-day	1982–2018	Attribution analysis
	ESA-CCI	VT	300m, annual	1992–2020	Vegetation functional types; attribution analysis
Socioeconomic	GlobPOP and Gridded GDP	PD and GDP	30 arc-sec, annual	1990–2022	Attribution analysis
	MVNL	NL	500 m, annual	1992–2022	Attribution analysis
	GRIP	R_{dis} and R_{dens}	Vector	Static	Attribution analysis
	Human activity intensity	HAI	300 m	1990–2020 (5-year intervals)	Attribution analysis
Geographic	GTOPO30	DEM, Slope, Aspect	1 km	Static	Attribution analysis
	IPCC Regions	Regional boundaries	Vector	Static	Regional stratification
Biodiversity	Global biodiversity grid	N, ASI, ASL, ASR	Vector	Static	Attribution analysis

Supplementary Tab. 2 Classification scheme for MetCDHI and SoilCDHI.

Classification	MetCDHI	SoilCDHI	Percentile change
None	> -0.5		30 ~ 100
Mild	-0.5 ~ -0.8		20 ~ 30
Moderate	-0.8 ~ -1.3		10 ~ 20
Severe	-1.3 ~ -1.6		5 ~ 10
Extreme	> -1.6		2 ~ 5

Supplementary Tab. 3 Candidate predictors used in the attribution analysis for divergent vegetation responses to SoilDH versus MetDH.

Category	Predictor Group	Variables Included	Description
Background environmental conditions	Climatic Background	PRE, ET, PET, SR, T, VPD, RH	Long-term mean hydroclimatic conditions
	Soil properties	SM, ST, SBD, SAND, SILT, CLAY, pH, CEC, OCC, CNR	Soil properties governing water retention, nutrient availability, and thermal regimes
	Event characteristics	Frequency, duration, and intensity (MetDH vs. SoilDH)	Long term average frequency, duration, and intensity of MetDH and SoilDH
	Topography	DEM, Slope, Aspec	Topographic constraints on water redistribution and microclimate
Vegetation state	Vegetation type	VT	Categorical classification of dominant vegetation functional type
	Vegetation structure & function	NDVI, LAI, GPP, NPP	Long-term mean canopy greenness, structure, and productivity
Hydro-Climatic anomalies	Water & energy anomalies	ΔPre, ΔET, ΔPET, ΔSR	Deviation of water and energy fluxes during the vegetation response period (SoilDH vs. MetDH)
	Thermal & moisture anomalies	ΔT, ΔST, ΔRH, ΔVPD, ΔSM	Deviation of temperature and moisture conditions during the vegetation response period (SoilDH vs. MetDH)
	Differences in drought-hot stress	ΔDuration, △Intensity	Deviation of event characteristics during the vegetation response period (SoilDH vs. MetDH)
Anthropogenic activities	Human footprint	HAI, PD, GDP, NL, Rdis, Rdens	Multi-dimensional intensity of human activities and infrastructure
	Biodiversity	N, ASI, ASL, ASR	Native and anthropogenic components of species richness

Notes: △X denotes the difference in the residual of variable X during the vegetation response period between SoilDH and MetDH.

Supplementary Tab. 4 Screening status of candidate predictors for the three response metrics.

Predictor variables set	$\triangle T_{res}$		$\triangle T_{rec}$		$\triangle Loss_{max}$	
	Iteration	VIF	Iteration	VIF	Iteration	VIF
△Duration	×	×	×	×	×	×
△ET	√	1.91	√	1.58	√	1.93
△Intensity	√	3.33	√	3.59	×	×
△PET	×	×	√	2.89	√	2.19
△PRE	√	1.42	√	1.42	×	×
△RH	×	×	×	×	×	×
△SM	√	3.02	√	3.10	√	2.81
△SR	√	1.94	√	1.97	×	×
△ST	√	3.09	√	2.75	√	3.10
△T	√	1.30	√	1.30	√	1.30
△VPD	√	3.67	×	×	√	3.98
ASI	√	2.63	√	2.91	√	2.91
ASL	√	2.04	√	2.29	√	2.41
Aspect	×	×	√	3.23	×	×
ASR	×	×	×	×	×	×
CEC	×	×	×	×	√	2.20
CLAY	×	×	7	8.93	×	×
CNR	×	×	×	×	×	×
DEM	√	2.10	√	2.24	√	2.10
MetCDHI_Duration	2	54.32	×	×	1	54.89
SoilCDHI_Duration	×	×	3	29.51	×	×
ET	6	6.14	5	15.42	×	×
MetCDHI_Frequency	×	×	1	46.61	×	×
SoilCDHI_Frequency	4	19.96	×	×	×	×
GDP	√	1.33	√	1.38	×	×
GPP	√	1.01	√	1.01	×	×
HAI	×	×	√	4.20	√	3.42
MetCDHI_Intensity	×	×	×	×	×	×
SoilCDHI_Intensity	×	×	×	×	5	9.20
LAI	×	×	8	6.26	×	×
N	×	×	×	×	×	×
NDVI	×	×	×	×	×	×
NL	√	1.50	√	1.56	√	1.54
NPP	×	×	×	×	×	×
OCC	√	1.57	√	1.65	×	×
PD	√	1.36	√	1.49	√	1.38
PET	√	2.40	√	2.95	×	×
PH	5	8.23	2	35.97	2	27.78
PRE	×	×	×	×	√	2.51
Rdens	√	1.57	√	1.63	√	1.62
Rdis	√	1.50	√	1.59	√	1.48
RH	×	×	×	×	×	×
SAND	×	×	6	13.31	×	×
SBD	1	123.44	×	×	×	×
SILT	×	×	×	×	4	12.85
Slope	√	1.99	√	2.05	√	2.16
SM	×	×	4	26.42	3	19.94
SR	3	30.42	×	×	×	×
ST	×	×	9	5.89	×	×
T	×	×	×	×	×	×
VPD	×	×	×	×	√	2.36
VT	×	×	10	5.01	6	5.16

Note: × indicates variables excluded during Step 1 and Step 2. Numbers indicate the removal iteration in the stepwise VIF procedure (Step 3), with the corresponding VIF value at removal shown in the adjacent column. √ indicates variables retained in the final predictor set (VIF < 5), with the final VIF value shown in the adjacent column.

Supplementary Tab. 5 Tuned hyperparameter configurations for each model, with default values omitted.

Model	Hyperparameter	Tuned result	Model	Hyperparameter	Tuned result
MLR	fit_intercept	TRUE	RF	n_estimators	500
	copy_x	TRUE		max_depth	15
	n_jobs	None		min_samples_split	4
	positive	FALSE	XGBoost	learning_rate	0.007
SVR	C	80		max_depth	7
	gamma	0.02		n_estimators	8200
	kernel	rbf			

Supplementary Tab. 6 Generalization performance of five regressors across △Tres, △Trec, and △Lossmax prediction tasks.

Model	Category	Task	Training R^2	Testing R^2	Training RMSE	Testing RMSE
XGBoost	Tree-based	$\triangle T_{res}$	0.949	0.800	0.027	0.105
		$\triangle T_{rec}$	0.958	0.863	0.057	0.185
		$\triangle Loss_{max}$	0.944	0.817	0.066×10^{-4}	0.216×10^{-4}
RF	Tree-based	$\triangle T_{res}$	0.649	0.560	0.186	0.231
		$\triangle T_{rec}$	0.792	0.731	0.281	0.362
		$\triangle Loss_{max}$	0.719	0.634	0.335×10^{-4}	0.432×10^{-4}
MLR	Linear	$\triangle T_{res}$	0.269	0.244	0.388	0.398
		$\triangle T_{rec}$	0.447	0.446	0.748	0.746
		$\triangle Loss_{max}$	0.223	0.216	0.927×10^{-4}	0.924×10^{-4}
SVM	Kernel	$\triangle T_{res}$	0.108	0.081	0.474	0.483
		$\triangle T_{rec}$	0.218	0.211	1.057	1.063
		$\triangle Loss_{max}$	0.066	0.067	1.111×10^{-4}	1.100×10^{-4}

Notes: The units of RMSE correspond to those of the predicted target variables. Specifically, $\triangle T_{res}$ and $\triangle T_{rec}$ are expressed in months, while $\triangle Loss_{max}$ is a dimensionless metric, thus its RMSE values have no units.

Supplementary Tab. 7 Goodness-of-fit indices of the PLS-SEM assessing drivers of divergent vegetation responses to SoilDH versus MetDH.

Response variable	GFI	SRMR
ΔT_{res}	0.915	0.063
ΔT_{rec}	0.941	0.042
$\Delta Loss_{max}$	0.932	0.047
Acceptance criterion	> 0.90	< 0.08